Journal of Oceanography (2023) 79:123–143
https://doi.org/10.1007/s10872-022-00671-4

ORIGINAL ARTICLE

Long-term sea-level variability along the coast of Japan during the 20th century revealed by a 1/10° OGCM

Hideyuki Nakano[1] · Shogo Urakawa[1] · Kei Sakamoto[1] · Takahiro Toyoda[1] · Yuma Kawakami[1] · Goro Yamanaka[1]

Received: 1 June 2022 / Revised: 29 October 2022 / Accepted: 8 November 2022 / Published online: 29 November 2022

Abstract

We explore long-term sea-level variability along the coast of Japan during the 20th century, using a 1/10° ocean general circulation model driven by two 20th century atmospheric reanalysis data. The modeled sea level anomalies along the coast of Japan (JPN-SLAs) show a consistent upward trend throughout the 20th century, which is comparable to global-mean sea-level rise, whereas no trend is obvious for the observed JPN-SLAs based on tide gauge data carefully selected by the Japan Meteorological Agency (JMA). We point out that the major difference between the model results and the tide gauge data may be due to the vertical land movements (VLMs) at the tide gauge stations, despite the JMA's assumption that the VLMs are relatively small there. If this is correct, the estimates from our model combined with the barystatic component by a recent study would yield a linear trend of 1.79 [0.89~2.28] mm yr^{-1} for JPN-SLAs without VLMs from 1900 to 2010, which is close to the global average SLAs estimated in recent studies. The empirical orthogonal function (EOF) analysis shows that the first mode of the modeled JPN-SLAs is almost spatially uniform with a peak in the 1950s. The peak is created by coastal trapped waves (CTWs), which are excited when positive sea level anomalies produced by change in wind stress, propagate westward as baroclinic Rossby waves and reach Japan. From idealized experiments, we find that the first EOF mode is well reproduced by the CTWs excited east of Hokkaido.

Keywords Sea-level anomalies · Japan coast · A 1/10° resolution model

1 Introduction

One of the most direct and significant impacts of global warming on human life is the sea-level rise. It is very important to investigate the impact of this phenomenon in Japan, where major cities are located in coastal areas. Understanding of sea-level processes along the coast of Japan is therefore necessary for proper coastal management against the sea-level rise. Hereafter, we will refer to the sea level anomalies along the coast of the four main islands of Japan as JPN-SLAs.

The longest record of the direct observations of the JPN-SLAs is conducted by the tide gauge stations. Note that sea-level records obtained from a tide gauge actually correspond to relative SLAs, that is, anomalies in the local mean sea level relative to the local solid surface at the tide gauge station. Therefore, the large influence of crustal deformation in Japan makes it very difficult to estimate the sea level variations accurately by the use of tide gauge data.

Under such circumstances, the Japan Meteorological Agency (JMA) has been trying to compile tide gauge data with great difficulty to monitor long-term variations of sea level along the coast of Japan. Okumura and Hirahara (2016) reviewed the their two process as follows. First, the JMA (2004, 2013) examined the annual-mean change of relative SLAs among the tide gauge stations with records for the past 100 years, and selected four tide gauge stations (Oshoro, Wajima, Hamada, Hososhima) that are supposed relatively stable with no clear ground motion or land subsidence (Fig. 1). Here, the relative SLAs are defined as the deviations from the 1981–2010 mean, which is the 30-year standard reference period for 1906–2020 data. We use the bracket to show the average of the relative JPN-SLAs at the four tide gauge stations as $[\text{ JPN-RSLA } (t)]_4$.

Second, JMA (2013) also selected new 16 tide gauge stations where VLMs are supposed to be within ±2 mm per year for the time record since 1960. For the estimation of

✉ Hideyuki Nakano
hnakano@mri-jma.go.jp

[1] Meteorological Research Institute, 1-1 Nagamine, Tsukuba, Ibaraki, Japan

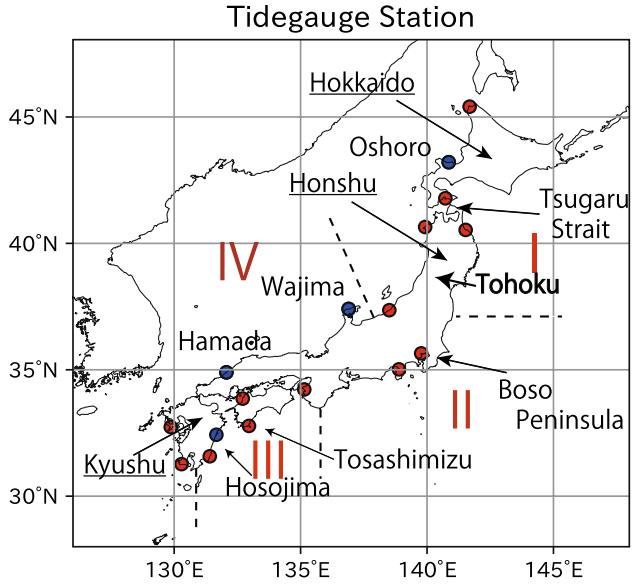

Fig. 1 The location of the tide gauge stations. Four tide gauge stations (blue) from 1906 to 1959 and 16 stations (red and blue) after 1960 are used for the JPN-SLA calculation. However, Hosojima is not included in the 16 stations in blue. For period from 1906 to 1959, the average of four blue stations are used for JPN-SLAs. For the period after 1960, the area around Japan is divided into four regions: I: the coast of Hokkaido and Tohoku, II: Kanto and Tokai, III: the Pacific coast of Kinki~Kyushu, and IV: the East China Sea coast of Hokuriku~Kyushu. The JPN-SLAs are calculated as the average of the annual mean sea level anomalies calculated for each of these areas. Hokkaido, Honshu, and Kyushu are three of four main islands of Japan and underlined. Tohoku is the name of northernmost six prefectures of Honshu

VLMs, they used the method of Kato and Tsumura (1979). In their method, tide gauge stations are divided into 58 regions, and the effect of sea conditions are removed by focusing on the fact that their anomaly components are common within the regions, and then sea level pressure (SLP)-corrected tide gauge data are supposed to be VLMs. The selected 16 tide gauge stations are divided into the four regions (region I to region IV in Fig. 1). The annual-mean relative SLA of each tide gauge data is averaged for each region, then finally, the relative SLA for each region is averaged, and the resulting time series is used as the long-term change in sea level along the coast of Japan. We refer to this as $[\,\text{JPN-RSLA}\,(t)]_{16}$. It is also found that the 5-year running means of $[\,\text{JPN-RSLA}\,(t)]_4$ and $[\,\text{JPN-RSLA}\,(t)]_{16}$ are almost identical (red thick line and blue thick line in Fig. 2). The agreement between the two may imply the assumption of small VLMs seems valid at these locations, but this is not necessarily the case. For example, the 5-year running mean of the relative SLA at Hamada reaches more than 100 mm in 2018 while that at Oshoro is less than 10 mm. Without taking VLMs into account, this is a large difference that cannot be explained simply by regional differences in SLA. This will be discussed in detail later.

The 5-year running means of $[\,\text{JPN-RSLA}\,(t)]_4$ and $[\,\text{JPN-RSLA}\,(t)]_{16}$ show an upward trend since the 1980s, with no upward trend in the period 1906–1980s (Fig. 2). In addition, throughout the entire period, there are decadal-scale variations and a multidecadal variations. The most striking feature of the 5-year running-mean of the relative JPN-SLAs is a multidecadal variation with an amplitude

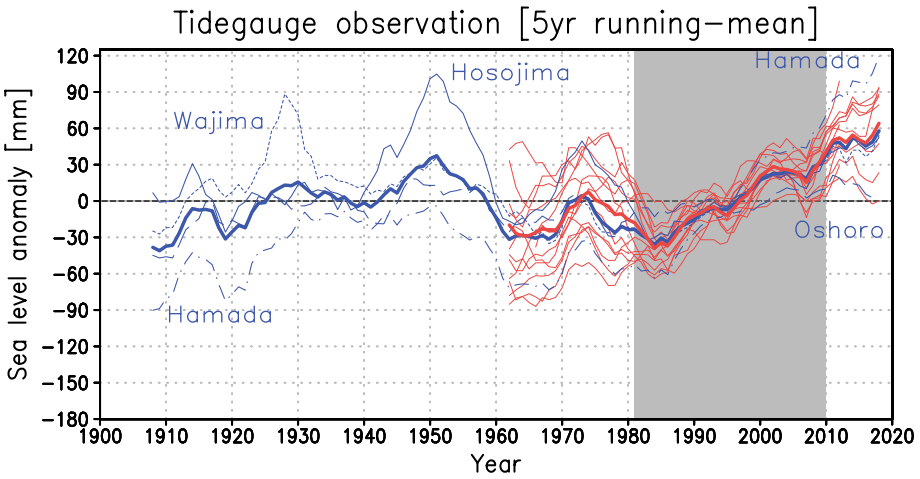

Fig. 2 Relative SLAs along the coast of Japan estimated by the tide gauge stations. Unit is mm. The average value from 1981 to 2010 is used as reference. The thick line shows the 5-year running mean of the average of the relative SLAs at four tide gauge stations (blue) and 16 tide gauge stations (red). The thin, dot-dashed, dotted, long-dashed blue lines indicate the relative SLAs at Hosojima, Hamada, Wajima, and Oshoro, respectively. The red thin line shows the relative SLAs estimated at each tide gauge station for the 16 station after 1960. The date observed at five tide gauge stations (Hakodate, Fukaura, Kashiwazaki, Tokyo, and Hachinohe), which were affected by 2011 earthquake off the Pacific coast of Tohoku, are not used since 2011. The vertical axis is set to be the same as that in Fig. 3 for comparison. The gray shade indicates the period from 1981 to 2010, the period for calculating the reference value

of 40 mm: a rise over 80 mm from 1900 to the 1950s, a decrease over 80 mm from the 1950s to the 1980s, and a rise over 100 mm from the 1980s to the present day (Fig. 2). The peak around the 1950s is so large that it was only exceeded after 2010. Apart from that, each peak is not much larger than the peak in the 1970s. The multidecadal variation is accompanied by decadal variations with an amplitude of 10–30 mm. It is also interesting to note that no upward trend is seen over the period (1906–1980s) unlike the SLAs in other region of the global ocean (GSLAs), although the upward trend of the relative JPN-SLAs since the 1980s to the present is consistent with GSLAs (JMA 2021). Therefore, it is very important to clarify the formation mechanism of the multi-decadal variations, which seems unique to Japan. However, since it is not easy to capture the entire multidecadal-scale variation, as a first step to analyze the entire multidecadal-scale variation, here we will revisit the 1950 variation that has been studied in the past, although it is only a part of multidecadal-scale variation.

The pioneering work on the formation mechanism for the relatively high JPN-SLAs in the 1950s was done by Sasaki et al. (2017). They used a 1° regional ocean general circulation model (OGCM) forced by a reanalysis-based atmosphere data set to obtain a time series of modeled JPN-SLAs similar to that of the relative JPN-SLAs. They proposed that the relatively high JPN-SLAs in the 1950s can be explained by the westward propagation of positive SLAs as baroclinic Rossby waves, which are produced by changes in wind stress due to the weakening of the Aleutian Low associated with the negative phase of the Pacific Decadal Oscillation (PDO). Their explanation is plausible, and we adopt part of this explanation in our study. However, we find it insufficient to explain why no trend is seen throughout the 20th century and how the Rossby wave excitation produces the JPN-SLAs. These problems are partly due to the coarse resolution of their model and not covering the global ocean.

In this study, we complement the work of Sasaki et al. (2017) as follows. First, we implement more sophisticated procedures for simulating JPN-SLAs. A realistic representation of the Kuroshio Extension and other currents around Japan, which are closely related to JPN-SLAs, requires a minimum horizontal resolution of about 1/10°, as noted by Kiss et al. (2020). In addition, a proper representation of coastal trapped waves (CTWs) requires a minimum resolution of 1/10° so as to (marginally) resolve continental shelves (Hughes et al. 2019). Therefore, we use an OGCM with a horizontal resolution of 1/10° for the Pacific model, which is nested in a global model, to evaluate a global thermosteric process and to represent JPN-SLAs more realistically. The OGCM is forced by two reanalysis-based atmospheric data sets to alleviate the problem of uncertainty in atmospheric data sets in the early 20th century.

Second, we take the effect of vertical land movements (VLMs) into consideration. In the study of Sasaki et al. (2017), there is no discussion of the effect of VLMs, but it is a significant impact with respect to JPN-SLAs (Okumura and Hirahara 2016). The large regional and temporal variability of the VLMs in Japan makes it difficult to assess it, even in the presence of a relatively dense global GPS network (Naito et al 2015). Here, we examine the time series of the standard deviation at each tide gauge station from their mean to estimate the effect of the VLMs.

Third, we intend to clarify how the Rossby wave excitation actually produces the JPN-SLAs. So far, we have considered JPN-SLAs to be spatially uniform. In fact, as we will show later in the model results, the SLA estimates do not differ much along the coast of Japan in terms of annual averages. This is generally attributed to uniformity of JPN-SLAs associated with the propagation of CTWs (Hughes et al. 2019). However, it is not easy to understand how CTWs uniform SLAs along the coast of Japan, which includes continental shelves and multiple straits, as well as the Japan islands. We will attempt to clarify the role of CTWs in the formation of the relatively high JPN-SLAs in the 1950s as an example. Although this model can (marginally) represent CTWs, the signal is a very fast-adjusting phenomenon that is concentrated in a narrow coastal area and is hidden by various other signals in the OGCM. Here, to evaluate the effect of CTWs more clearly, we conduct a series of idealized experiments using the same model resolution and topography.

The rest of the paper is organized as follows. Section 2 describes the model and experimental method. Section 3 presents the time series of JPN-SLAs in the hindcast experiments. Section 4 examines spatial patterns of the modeled JPN-SLAs targeting their relatively high values in the 1950s. After confirming the findings by Sasaki et al. (2017) for the relatively high JPN-SLAs, we will analyze it especially in terms of CTW dynamics. We conclude with a brief summary in Sect. 5.

2 Model and experimental method

2.1 OGCM

The OGCM used in this study is the Meteorological Research Institute Community Ocean Model (MRI.COM: Tsujino et al. 2017). MRI.COM is a depth coordinate model that solves the primitive equations under hydrostatic and Boussinesq approximations. Using a two-way nesting method, a 1/11° ×1/10° North Pacific (NP) model is nested in a 1°×0.5° global ocean model, where the vertical resolution is 60 levels, and the minimum water depth is 8 m. The domain of the NP model is 99°E-75°W, 15°S-63°N. The

configurations of the global and NP models are the same as those of Sakamoto et al. (2019) and Nakano et al (2021). Table 1 summarizes the configurations of the NP model. Basic performance of this NP model is presented in Nakano et al (2021).

2.2 Hindcast experiments

To evaluate the SLAs from the early 20th century to the present, we performed two hindcast experiments using two reanalysis-based data sets: the 20CRv3 data set (Slivinski et al. 2019) and the ERA20C data set (Poli 2016), which cover the whole 20th century. The time interval of these dataset is 3 h. We made some modifications to the reanalysis data in the following. We use a climatology data for runoff, because no suitable data is available. The climatology data is created from JRA55do (Tsujino et al. 2018) daily averaged dataset during 1988–2017 (Suzuki et al. 2018) by applying a Kolmogorov-Zurbenko filter (a nine-day running-mean three times). We also add an offset of +1 °C to the surface air temperature to alleviate a known cold bias in ERA20C, following Kusahara (2020). The impact of these modifications on sea levels is expected to be small.

Hindcast simulations require initial conditions; however, initial ocean data for the first half of the 20th century do not exist. Even if they did exist, it would be necessary to spin up the model in order to reduce a long-term drift of ocean temperature and salinity. We create the initial state for the early 20th century by repeatedly using data from the early 1900s, when the post-industrial effects are weak. For the repetition period, we choose the years 1900-1929 for each dataset, following Kusahara (2020). Due to the limitation of computational resources, the preindustrial initialization phase is performed using the global model only. Starting from the World Ocean Atlas 2013 version 2 (WOA13v2, Boyer et al. 2013), we apply 16 cycles of 1900–1929 in the 20CRv3 and ERA20C data sets. By repeating the 1900–1929 period for 16 cycles, the trend of the global-mean temperature is suppressed to less than 0.01°C for 300 years. After the spinup integration, using the NP model nested in the global model, we carry out a hindcast simulation with interannually varying surface boundary conditions for the period 1871–2015 for 20CRv3 and 1900–2010 for ERA20C. Hereafter, we call the two hindcast experiments exp 20CRv3 and exp ERA20C, respectively. We examine only the results of the NP model and omit using NP in indicating the NP model.

2.3 The method to estimate the SLAs in the model

A Boussinesq ocean model should be adjusted with a a globally uniform time-dependent factor to account for the global-mean SLAs due to changes in global mean thermodynamic contribution (e.g., Greatbatch 1994). The globally uniform factor is diagnostically calculated by the net expansion/contraction of the global ocean (e.g., Griffies and Greatbach 2012). As shown by Mellor and Ezer (1995), the globally uniform factor can correct a Boussinesq model on timescales longer than barotropic adjustments, so that it closely approximates the corresponding non-Boussinesq model.

Total SLAs are estimated as

Table 1 Main settings of the North Pacific model

Numerical model	MRI.COM
Coordinates	free-surface z^* coordinate (vertical) and polar coordinate (horizontal)
Region	99°–285°E, 15°S–63°N
Horizontal resolution	1/10° latitude and 1/11° longitude
Vertical resolution	2–700 m (60 levels) (minimum water depth of 8 m)
Grid size	$2049 \times 784 \times 60 = 963{,}849{,}600$
Tracer advection	SOM (Prather 1986) with a flux limiter (Merryfield and Holloway 2003)
Horizontal viscosity	Smagorinsky-like biharmonic (Griffies and Hallberg 2000) with additional harmonic viscosity near the lateral boundaries
Horizontal diffusion	biharmonic (diffusivity = 1.0×10^8 m^4 s^{-1})
Vertical turbulent mixing	GLS scheme (Umlauf and Burchard 2003) using the default coefficients of MRI.COM (Sect. 15.4 of Tsujino et al. 2017,)
Downscaling	two-way online double nesting method
Sea ice	5-category sea ice model (Mellor and Kantha 1989; Hunke and Dukowicz 1997, 2002)
Surface boundary	JRA55do ver.1.3 data. The bulk formula of Large and Yeager (2004) and the solar altitude scheme of Ishizaki and Yamanaka (2010) are used. A factor of 0.05 is applied to the first layer current vector of the ocean model before it is subtracted from the surface wind to compute the relative wind.
River runoff	JRA55do (Suzuki et al. 2018)
Relaxation condition	Sea-surface salinity is restored to monthly climatology with a piston velocity of 2 m per 14.6 days, and raised sharply when it falls below 10.

$$\mathrm{SLA}\ (x,y,t) = h_g(t) + \ \mathrm{SSHA}\ (x,y,t) + h_{ib}(x,y,t) + h_b(t), \tag{1}$$

where $h_g(t)$ is the global steric component of the SLAs, and SSHA(x, y, t) is modeled ocean dynamic sea-surface height anomalies (SSHAs) from the reference value and are stored in the diagnostic name `zos` in Coupled Model Intercomparison Project (CMIP). The third term, $h_{ib}(x,y,t)$, is the inverse-barometer component and can be diagnosed using sea level pressure (P_a) (Griffies and Greatbach 2012).

$$h_{ib} = \frac{\overline{P_a} - P_a}{g\rho_s} \sim -9.9\ \mathrm{mm/hPa} \times (1013\ \mathrm{hPa} - P_a), \tag{2}$$

where g is local gravity acceleration and ρ_s is the local surface density. Here following Gregory et al. (2019), we neglect the spatial variations in g and ρ_s, and replace them with a constant. We use a factor of −9.9 mm/hPa with a constant value for ρ and 1013.0 hPa for $\overline{P_a}$. The error in this case is less than 1%. The annual average of h_{ib} is about 0∼10 mm, although it can have a size of several tens of centimeters in typhoons and other cases. The last term of Eq. 1, $h_b(t)$, is the barystatic component, which is due to the addition to the ocean of water mass that existed on the land area, such as melting of glaciers. In general, it cannot be represented by OGCMs. Here, we use an estimate by Frederikse et al. (2020). We are not concerned with the place where the water mass is added to the ocean from the land but its total sum (Gregory et al. 2019).

The relative SLAs observed by the tide gauge station are the anomalies in local mean sea level relative to the vertical land movements (VLMs) at the tide gauge station. Therefore, to compare the modeled SLAs quantitatively with the relative SLAs, the following correction is necessary.

$$\frac{\partial}{\partial t}\ \mathrm{RSLA}\ (x,y,t) = \frac{\partial}{\partial t}\ \mathrm{SLA}\ (x,y,t) - \ \mathrm{VLM}\ (x,y,t) \tag{3}$$

where RSLA(x, y, z) is the relative sea-level anomalies, VLM(x, y, t) is the vertical land movements.

In the tide gauge estimate, most of uncertainty arises from VLMs. Part of VLMs is glacial isostatic adjustment, which is due to ongoing changes in the solid Earth caused by past changes in land ice. From Fig. 3a of Tamisiea and Mitrovica (2011), it is estimated as 0.1 ∼ 0.4 mm yr^{-1} around Japan. But in Japan, other contributions of VLMs are significant, and varies widely in space and time (Hammond et al. 2021, Naito et al. 2015). Okumura and Hirahara (2016) attempted VLM correction at several tide gauge stations that do not correspond to the 16 tide gauge stations listed above (e.g., listed in Fig. 1), and found that VLMs can reach as high as −3.4 to 8.5 mm yr^{-1}.

3 Time series of sea level anomalies along Japan (JPN-SLAs) in the hindcast experiments

3.1 Time series of JPN-SLAs

Next, we see the modeled JPN-SLAs in the hindcast experiments. The representative value for the modeled JPN-SLAs is the average of SLAs in Eq. (1) at the four model grids that correspond to the four tide gauge stations (Wajima, Hamada, Hosojima, and Oshoro). Since it is not possible to estimate barystatic sea-level rise ($h_b(t)$) in the model, we use one of the latest estimates based on Frederikse et al. (2020) as $h_b(t)$ and estimate the total JPN-SLAs (green line in Fig. 3). The modeled JPN-SLAs in both exp 20CRv3 and exp ERA20C are dominated by a positive trend in JPN-SLAs throughout the 20th century (Fig. 3), in contrast to [JPN-RSLA]$_4$ (Fig. 2) where no trend is visible in the period 1906–1980s. The modeled JPN-SLAs also show multi-decadal variation, as seen in the relative JPN-SLAs. The modeled JPN-SLAs have clear peaks similar to [JPN-RSLA]$_4$ in the 1920s, 1950s, 1970s, early 1990s, and early 2000s.

The global-mean steric sea-level rise ($h_g(t)$) accounts for a large proportion of the modeled sea-level rise in JPN-SLAs and difference in the long-term trend between the modeled JPN-SLAs and [JPN-RSLA]$_4$, so that we check the validity of our estimates by comparing them with those of previous studies (Table 2). We find that the rate of the sea-level rise due to the steric component has accelerated from 0.18 [0.09∼0.27] mm yr^{-1} during 1900–1971 to 0.92 [0.80∼1.05] mm yr^{-1} during 1971–2006. These values are consistent with the previous studies.

It is noted that the modeled JPN-SLAs by Sasaki et al. (2017) have no clear upward trend and are closer to the relative JPN-SLAs than those of our study. This is likely due to the fact that their estimate does not include a barystatic component and that their steric component is underestimated owing to the use of a regional model. As a result, their results show a relatively larger contribution from ocean dynamics than our results, resulting in apparently better agreement with the tide gauge estimates.

3.2 VLM impact evaluation in the tide gauge observation

If modeled steric sea-level rise and barystatic sea-level based on Frederikse et al. (2020) are reasonable, we should consider what mechanism would produce the difference between [JPN-RSLA]$_4$ and the modeled JPN-SLAs. One of the candidates is the effect of VLMs, which is known

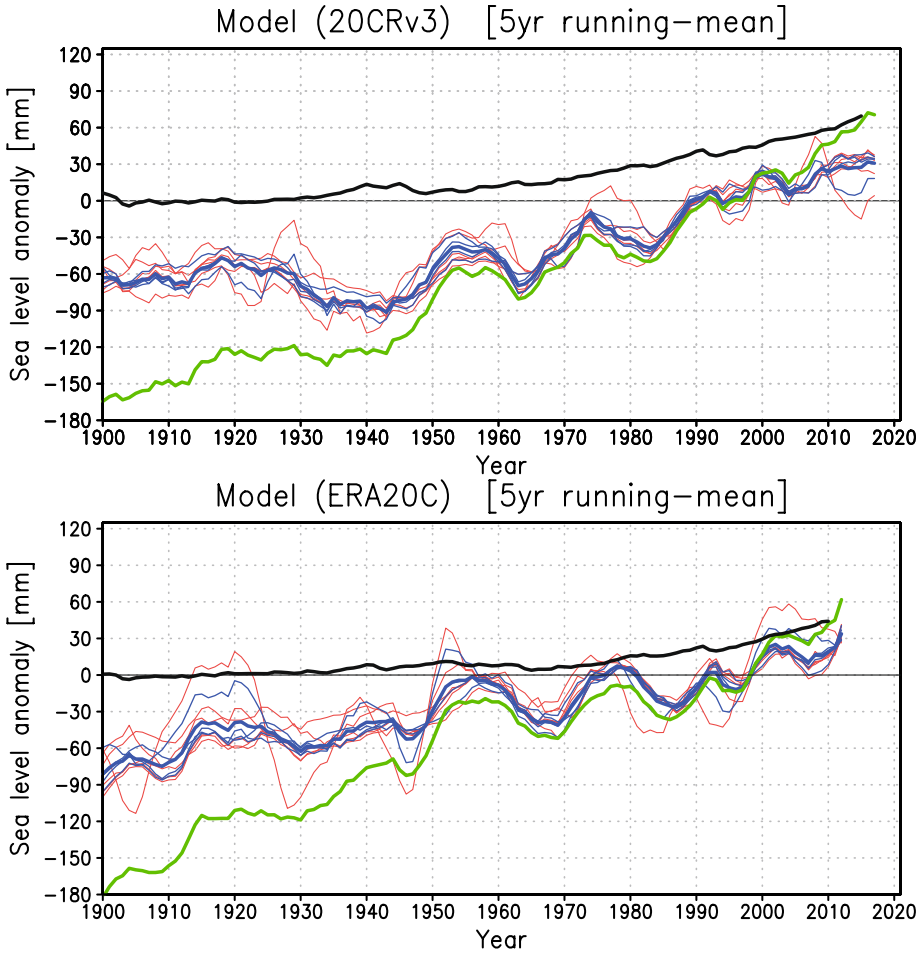

Fig. 3 Five-year running-mean JPN-SLAs (h_g + SSHA + h_{ib}) estimated at each of the four tide gauge stations (thin blue lines). Unit is mm. The reference is the average value obtained for the period from 1981 to 2010. Thick blue line is their average. Five-year running-mean JPN-SLAs at each of the twelve tide gauge stations are also shown in thin red lines. Five tide gauge stations (Hakodate, Tokyo, Uchiura, Wakayama, and Matsuyama) are excluded since they are located in the inner bay and cannot be well represented in the model. Green line shows the sum of the contribution of barystatic change ($h_b(t)$) based on Frederikse et al. (2020), that is, h_g + SSHA + h_{ib} + h_b. Black line shows the global mean thermodynamic contribution of only ($h_g(t)$). (**a**) exp 20CRv3. (**b**) exp ERA20C

to have very large spatial variation in Japan (Hammond et al. 2021). We attempt to examine the effect of VLMs by focusing on the fact that the relative SLAs at each tide gauge station deviates significantly from their average outside the period of 1981–2010 (Fig. 2), while the modeled SLAs at each tide gauge station are close to their average (Fig. 3).

We estimate time series of their standard deviation as a measure of the reliability of the averages in the following

$$\sigma_n(t) = \sqrt{\frac{1}{n-1}\sum_i (\text{ JPN-SLA}_i(t) - [\text{ JPN-SLAs }(t)]_n)^2}. \tag{4}$$

For both the 4-station estimate ($\sigma_4(t)$) and 16-station estimate $\sigma_{16}(t)$, the standard deviation shows a minimum value of about 20 mm around 1995, but reaches 60 mm outside that period (Fig. 4); the rate of increase of $\sigma_4(t)$ for 2011–2018 is 2.72 mm yr^{-1}. Even though the 4-station estimate ([JPN-RSLA $(t)]_4$) is similar to the 16-station estimate ([JPN-RSLA $(t)]_{16}$), the large deviation at each tide gauge station from their mean raises questions about the representativeness of the averages.

To illustrate this behavior, consider the following scenario where the VLMs at each tide gauge location (i) varies from place to place, but is constant with respect to time as C_i from 1970–2018. Since JPN-RSLA (t) is set to zero at the 1981–2010 average, the JPN-RSLA$_i$ due to the VLM$_i$ can be expressed this way,

$$C_i\left(t - \frac{t_1+t_2}{2}\right) \qquad (t_1 = 1981, t_2 = 2010). \tag{5}$$

Then the standard deviation of the JPN-RSLA due to the VLMs ($\sigma_v(t)$) is

$$\sigma_v(t) = \left|t - \frac{t_1+t_2}{2}\right| \sqrt{\frac{1}{n-1}\sum_i (C_i - [C]_n)^2}, \tag{6}$$

where $[C]_n$ is the mean of C_i among n gauge stations. Therefore, the total standard deviation is estimated by adding $\sigma_v(t)$ and the standard deviation with respect to oceanographic phenomenon in SLAs ($\sigma_0(t)$) in quadrature since both are considered independent.

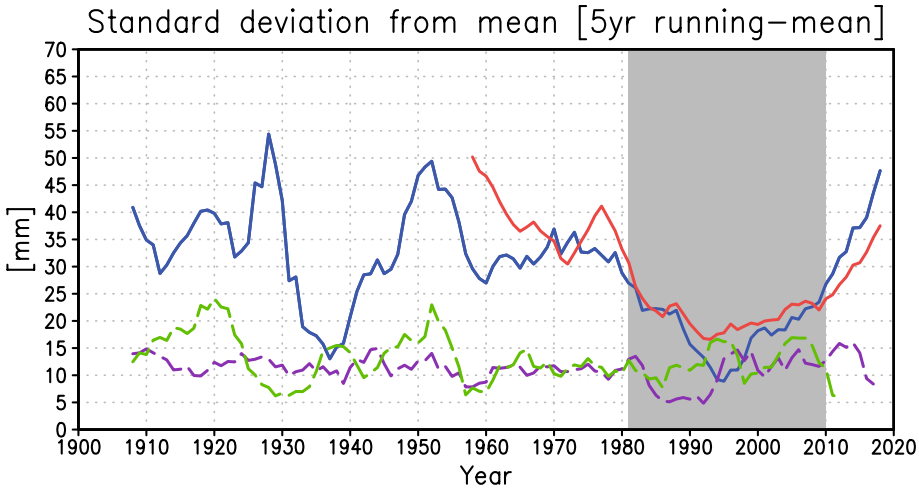

Fig. 4 Time series for the standard deviation of the 5-year running mean of relative SLAs at the tide gauge stations from its mean (blue line: $\sigma_4(t)$, red line: $\sigma_{16}(t)$). Unit is mm. The gray shade indicates the period from 1981 to 2010, the period for calculating the reference value. Purple and green dashed lines are modeled estimation for exp 20CRv3 and for exp ERA20C, respectively

$$\sigma(t) = \sqrt{\sigma_v(t)^2 + \sigma_0(t)^2} \tag{7}$$

If $\sigma_v(t) >> \sigma_0(t)$, then $(\sigma(t))$ will reach a minimum at $(t_1 + t_2)/2 = 1995.5$. This is consistent with Fig. 4. Based on the GPS based estimate of Hammond et al. (2021), VLMs in mm yr^{-1} at Oshoro, Wajima, Hamada, and Hosojima are 3.326 ± 0.531, -0.721 ± 0.412, -1.667 ± 0.335, and -3.092 ± 0.505, respectively. Using these value for C_i, $\sqrt{\frac{1}{n-1}\sum_i (C_i - [C]_n)^2}$ is estimated as 2.29–3.21 mm yr^{-1}. This is consistent with the rate of increase of $\sigma_4(t)$ for 2011–2018 (2.72 mm yr^{-1}). Hence the estimate in this scenario, where VLMs are constant over time, may explain part of $\sigma(t)$ after the 1950s, a period in which σ_4 increase as it leaves 1995 in Fig. 4.

Unfortunately, the GPS-based VLMs cannot explain the difference between the modeled JPN-SLAs and the relative JPN-SLAs during the 20th century. First, the average VLM estimated for the above four stations is −0.505 mm yr^{-1}. Correcting [JPN-RSLA $(t)]_4$ by this value using Eq. (3) results in a larger difference. Second, going back before 1960, $\sigma(t)$ shows a very irregular pattern. This is likely due to the irregular time variation of VLMs (Naito et al 2015). Actually, we can find an example of events with strong VLM influence; according to the study of VLMs by Kato (1983) (in his Fig. 4), there was sudden uplift of about 50 mm in 1957 at the Hosojima tide gauge station, which may cause too strong influence of Hosojima station for [JPN-RSLA$]_4$ in the 1950s (Fig. 2).

In summary, we cannot estimate the VLMs to correct [JPN-RSLA$]_4$ through the 20th century. Nevertheless, there is reasonable doubt that the tide gauge estimate includes VLMs, the value of which is comparable to the trend of the global averaged SLAs.

3.3 Linear trends of the modeled JPN-SLAs

As discussed in the Sect. 3.2, it is clear that the effect of VLMs is too large to be ignored. If this conclusion is correct, then this model estimate (Table 2) corresponds to the JPN-SLAs without VLMs from the beginning of the 20th century. The linear trend of JPN-SLAs in mm yr^{-1} is 1.79 [0.89~2.28] for 1900–2010 and 3.15 [1.89~4.13] for 1983–2010. These values are similar to the global averaged SLAs based on IPCC AR6 (Table 2). On the other hand, tide gauge values do not have clear upward trend in SLAs for 1900–2010 and 1900–1983. For 1900–1983, the trend of the barystatic component is dominant (~ 70%). For 1983–2010, the trends of the barystatic, steric, and other dynamical components have approximately similar magnitudes, indicating that dynamical SLAs (SSHAs), which are assumed to be zero in the long term, were also working to raise SLAs during this period.

To summarize, we showed that the relative JPN-SLAs did not show long-term trend throughout the 20th century (Table 2), whereas the modeled JPN-SLAs did a consistent upward trend. The VLMs are thought to be a major factor for this difference. If this conclusion is correct, then this model estimate without the VLMs is close to the global averaged SLAs estimated in recent studies (Table 2). Despite the large difference among the long-term trends, the modeled JPN-SLAs have distinct peaks similar to [JPN-RSLA$]_4$ in the 1920s, 1950s, 1970s, early 1990s, and early 2000s.

4 The spatial pattern of the modeled JPN-SLAs with respect to its peak in the 1950s

In this section, we investigate how the decadal variability of the JPN-SLAs is created, especially focusing on the peak in the 1950s. In the model, time series of SLAs at the

Table 2 Estimated linear trend of SLAs in hindcast experiments and tide gauge observations and AR6 with its 90% confidence interval

	1900–2010[a]	1900–1983	1983–2010	1900–1971[b]	1971–2006
Steric	0.42 [0.28~0.56]	0.23 [0.12~0.34]	1.06 [0.95~1.17]	0.18 [0.09~0.27]	0.92 [0.80~1.05]
Dynamic	0.39 [0.20~0.58]	0.33 [-0.2~0.87]	0.94 [0.40~1.48]	0.23 [-0.34~0.80]	0.24 [-0.4~0.87]
Barystatic[c]	0.98 [0.66~1.29]	1.21 [0.89~1.53]	1.15 [0.78~1.52]	1.40 [1.08~1.72]	0.75 [0.36~1.11]
Total	1.79 [0.89~2.28]	1.78 [0.53~2.73]	3.15 [1.89~4.13]	1.81 [0.52~2.82]	1.92 [0.56~3.03]
tide gauge	0.34 [-0.56~1.24]	0.03 [-0.70~0.76]	2.73 [0.13~5.34]	0.22 [-0.65~1.09]	0.80 [-1.50~3.10]
Steric (SROCC[d])					0.8 [0.5~1.1]
Steric (CMIP6[e])				0.2 [0.1~0.3]	
Steric (Frederikse, 2020)	0.48 [0.30~0.65]	0.40 [0.22~0.59]	0.90 [0.64~1.15]	0.38 [0.19~0.56]	0.70 [0.50~0.89]
Total (SROCC)	1.5[1.1~ 1.9]				
Total (AR6)				1.3 [0.6 ~ 2.1]	1.9 [0.8~2.9]

(a) The period for the tide gauge is 1906–2010 and that for Total (SROCC) is 1902–2010.

(b) The period for the tide gauge is 1906–1971 and that for Steric (SROCC) is 1900–1990.

(c) The barystatic component is based on Frederikse et al. (2020).

(d) Special Report on the Ocean and Cryosphere in a Changing Climate (IPCC, 2019)

(e) Based on Jevrejeva et al. (2021).

Unit is mm yr^{-1}. The dynamic component is the sum of the ocean dynamic sea-level change from the reference values and the inverse barometer effect, although the latter is negligibly small. The steric and dynamic trends are estimated using the annual averaged SLAs in both the exp 20CRv3 and exp ERA20C. We compute trends and their uncertainty for the barystatic sea-level change estimated by Frederikse et al. (2020) using their python scripts. Details are written in Appendix

corresponding four tide gauge stations are not very different (Fig. 3). To investigate how these nearly uniform values can be obtained, we examine the relatively high JPN-SLAs in the 1950s, which has been also investigated by Sasaki et al. (2017). We examine the spatial distribution of JPN-SLAs in detail, using the grid points of the model corresponding to the 77 tide gauge locations facing the open ocean in the Japan Islands (Fig. 5). In the following, we will examine the SLAs without modification of h_g, h_b, and h_{ib} to focus on dynamic variability; this is equivalent to examining SSHAs of the model.

4.1 An EOF analysis to the modeled JPN-SLAs

We perform the empirical orthogonal function (EOF) analysis using the 5-year running mean of the SSHAs for the period 1920–1970, during which multidecadal variation is particularly dominant. The first EOF mode (EOF1) represents a simultaneous rise and fall of the SSHAs along the coast of Japan except for the eastern coast of Hokkaido, explaining a 80.7% and 66.7% of the total variance for exp 20CRv3 and ERA20C, respectively (Figs. 5a, d). This is consistent with previous studies targeting decal to interannual JPN-SLAs variabilities (Senjyu et al. 1999). The times series of this mode show relatively low values during 1940–1945 and relatively high values around 1955, largely explaining the modeled peak in JPN-SLAs during the 1950s.

The correlation of SSHAs in the northwest Pacific to EOF1 is uniformly high in the vicinity of Japan (Fig. 6a, b). In addition, the Japan Sea and the East China Sea also show uniformly high correlations, suggesting that there is a fast adjustment due to the barotropic Rossby waves generated from the western coast of Japan as the CTWs move northward along the coast (Kida et al. 2016). In the Sect. 4.2.2, we will conduct a series of idealized experiments to confirm that these high correlations can actually be explained by CTWs and Rossby waves. In the Pacific Ocean to the east of Japan, the correlation is almost uniformly positive except for the Kuroshio, the Kuroshio Extension, south of the Kuroshio Extension, and the Sea of Okhotsk. These patterns are very similar to those of exp 20CRv3 and exp ERA20C, suggesting that there is not much uncertainty in the external forcings that produce the large-scale SSHAs in the Pacific.

The regression of SSHAs against EOF1 shows a similar pattern to the correlation, but the values in the open ocean are generally larger than those along the coast, suggesting that the signal is smoothed and reduced in coastal areas than in the open ocean (Figs. 6c, d). The major signals that stand out are the north-south dipole structure across the Kuroshio Extension (140°–160°E, 35°N for 20CRv3 and 33°N for ERA20C) and the large positive values in a wide range of 35°N–45°N. The former suggests that the SSHAs associated with the meridional movement of the Kuroshio and Kuroshio Extension are one of the important sources of CTWs. This is consistent with studies by Sasaki et al. (2014) and Usui et al. (2021) showing westward propagation of the Kuroshio-induced CTWs along the south coast of Japan. However, as will be discussed later, the influence of the positive SSHAs, represented by large positive values in the wide range

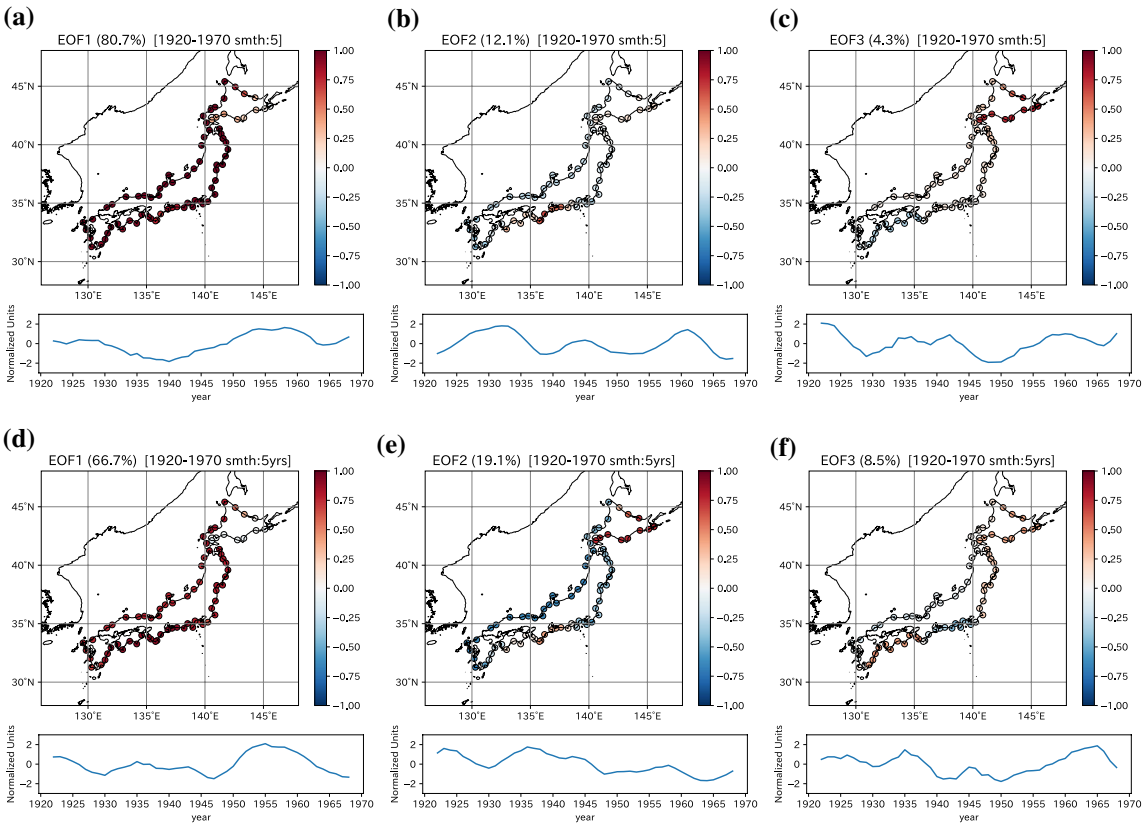

Fig. 5 Principal component of the EOF modes for the modeled SSHAs at the 77 tide gauge stations (open circles). **a**, **d** The first EOF mode, **b**, **e** the second EOF mode, and **c**, **f** the third EOF mode for **a**–**c** exp 20CRv3 and for **d**–**f** exp ERA20C

Fig. 6 Correlation and regression coefficients of SSHAs to the time series of the first EOF mode in Fig. 5. Unit of correlation is none. Unit of regression is mm. Correlation coefficient for (**a**) exp 20CRv3 and (**b**) exp ERA20C. Regression coefficient for (**c**) exp 20CRv3 and (**d**) exp ERA20C

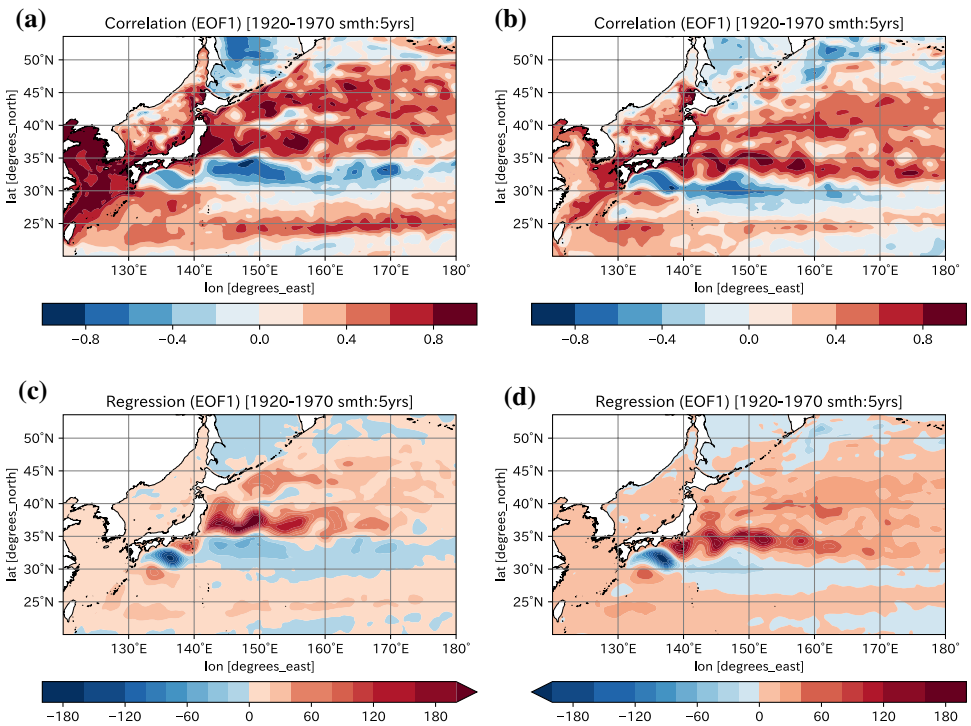

of 35°N–45°N, is larger than these contributions, suggesting that largest regression area does not necessarily mean the most contributing one.

The contribution of the second EOF (EOF2) to the total variance is greatly reduced compared to that of EOF1, being 12.1% and 19.1% of the total variance for 20CRv3 and ERA20C, respectively (Figs. 5b, e). The EOF2 is represented by a positive value from Shikoku to the Izu Peninsula and a generally weak negative signal along the rest of the Pacific coast (Fig. 7). In 20CRv3, the positive signal is stronger east of Cape Shionomisaki, especially in ERA20C, while the negative signal is stronger along the east coast of Hokkaido. There is a strong positive signal on the east coast of Hokkaido. The correlation and regression of the EOF2 are quite different among exp 20CRv3 and exp ERA20C. In exp 20CRv3, the positive correlation is associated with the northward movement of the Kuroshio Extension. On the other hand, in exp ERA20C, the positive correlation and regression show a clear pattern along the south coast of Japan, which is generally consistent with the pattern of large meanders and non-meanders. This time series does not correspond well to the meandering and non-meandering phases in the real ocean. The modeled meandering period is estimated to be 1928–1932, 1948–1968, when EOF2 is negative in exp ERA20C. In the real Kuroshio, it is estimated to be 1933–1943, 1953–1956, and 1959–1963 (Nyomura 2010).

The contribution of the third EOF mode (EOF3) to the total variance is even lower than the second mode, at 4.3%, and 8.5% for exp 20CRv3 and exp ERA20C (Fig. 5c, f). The pattern is then further subdivided and separated regionally (Fig. 8). Correspondingly, the correlation and regression show that the north-south width of the pattern is clearly shorter than that of EOF1 and EOF2.

Not only is the power of the first EOF mode much higher than the other modes, but it is also much more robust to the two external forcings of 20CRv3 and ERA20C. In addition, this mode seems to produce the most prominent peak in the 1950s in the long-term SSHAs in Japan. In comparison, the correlation patterns to the second and third EOF modes are quite different among exps 20CRv3 and ERA20C, indicating they are not robust modes. Therefore, we will focus on the first EOF mode in the following analysis.

4.2 Idealized experiments

4.2.1 Experiment using a 1.5-layer reduced gravity model

Sasaki et al. (2017) pointed out that the peak of the long-term variability (> 50 years) seen around 1950s was due to changes in wind stress, which corresponded to the weakening of the Aleutian Low. Actually, in exp 20CRv3 and exp ERA20c, the positive SSHAs propagating from the central Pacific reach the east coast of Japan in the late 1950s (Fig. 9). To confirm the importance of wind stress, we run a 1.5-layer reduced model with 20CRv3 and ERA20C wind stresses. The settings of the shallow water model are

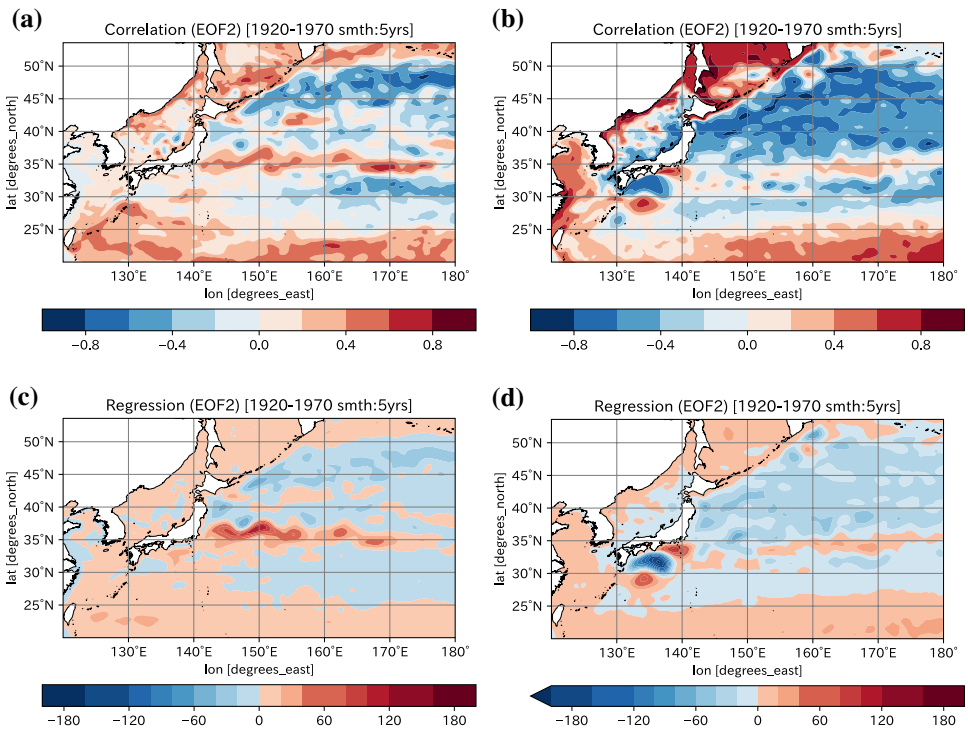

Fig. 7 Same as Fig. 6 but for the second EOF mode

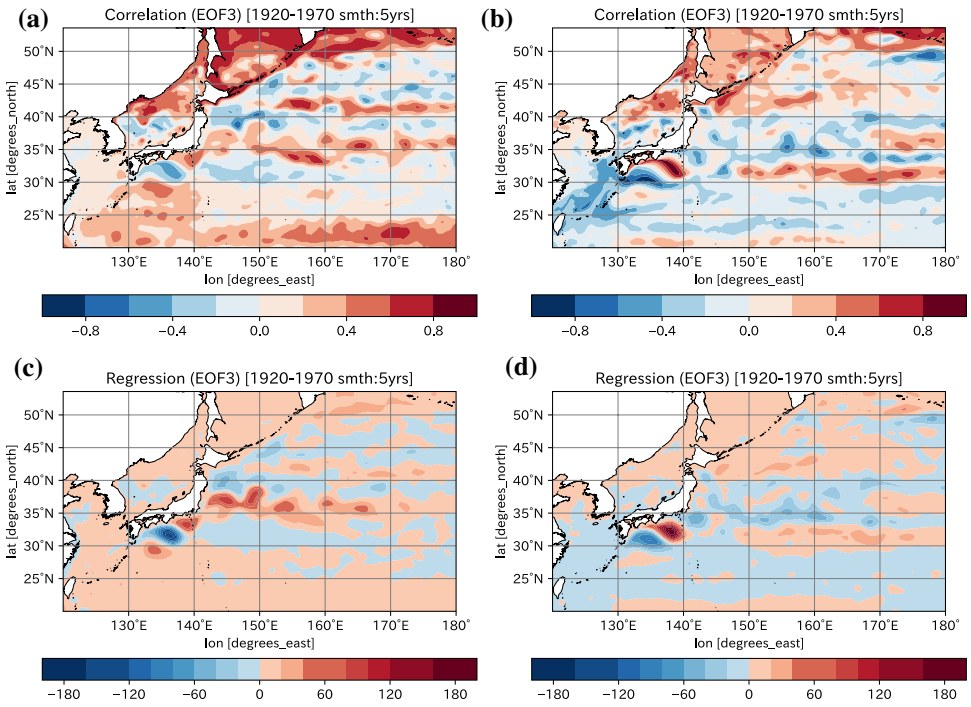

Fig. 8 Same as Fig. 6 but for the third EOF mode

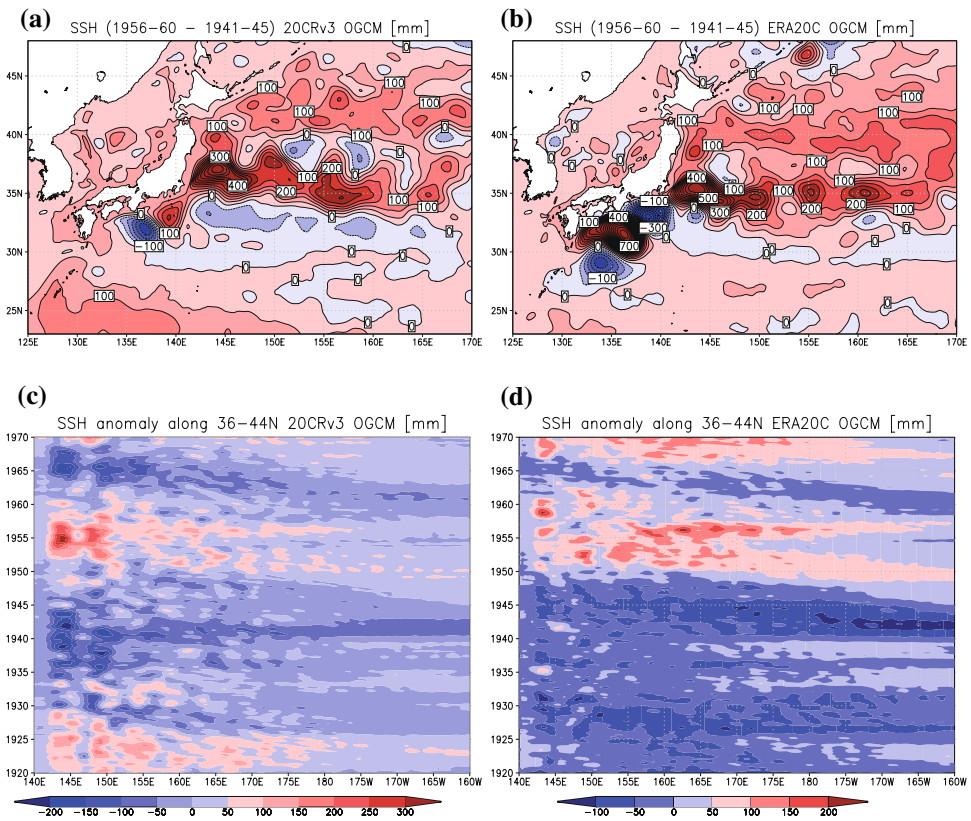

Fig. 9 SSHA obtained in the OGCM experiments. Unit is mm. **a** SSH difference between 1941–1945 average and 1956–1960 average ($\overline{\mathrm{SSH}}^{1956-1960} - \overline{\mathrm{SSH}}^{1941-1945}$) in exp 20CRv3. **b** Same as **a** but for exp ERA20C. (c) Longitude-time plots of SSHAs averaged in 36°–44°N in exp 20CRv3. **d** Same as **c** but for exp ERA20C

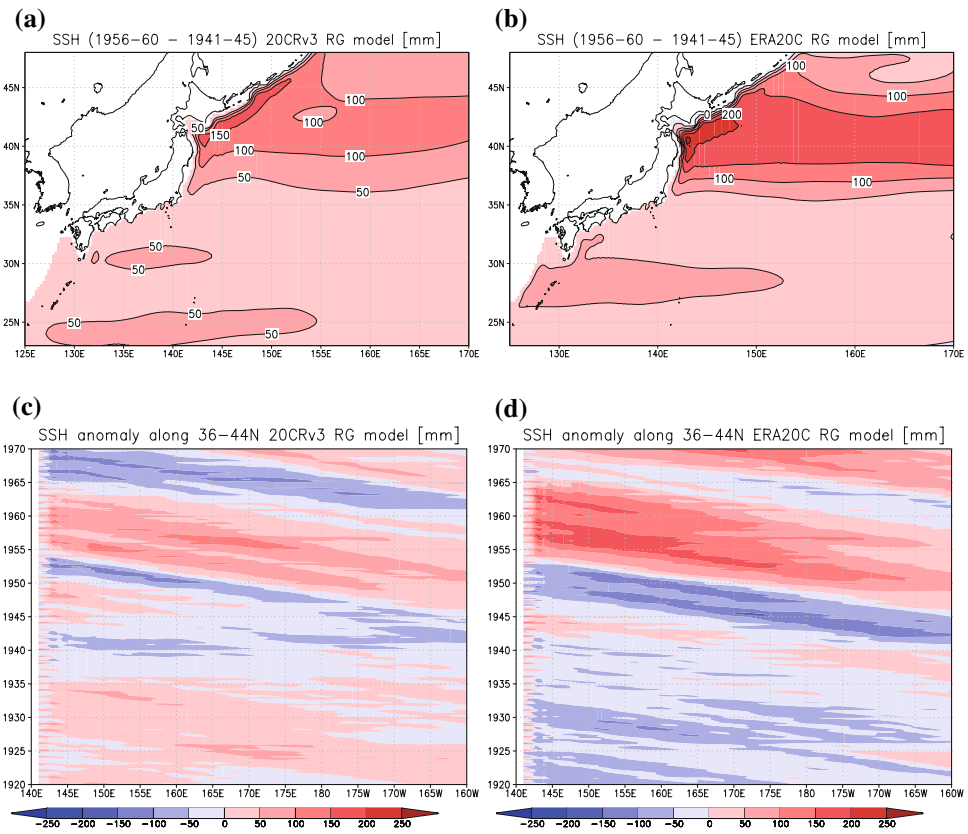

Fig. 10 SSHA obtained in a shallow water model. Unit is mm. **a** SSH difference between 1941–1945 average and 1956–1960 average ($\overline{\mathrm{SSH}}^{1956-1960} - \overline{\mathrm{SSH}}^{1941-1945}$) in the shallow water model using the wind stress of exp 20CRv3. **b** Same as **a** but for exp ERA20C. **c** Longitude-time plots of SSHAs averaged in 36°–44°N in the shallow water model using the wind stress of exp 20CRv3. **d** Same as **c** but for exp ERA20C

the same as those used in Yamanaka et al. (2021), except for the wind forcings.

In both experiments using 20CRv3 and ERA20C wind stresses, we find that positive SSHAs propagating from the central Pacific reach the east coast of Japan in the late 1950s (Fig. 10). This is consistent with the results of Sasaki et al. (2017). The amplitude is particularly large from Tohoku to Hokkaido, reaching about 200 mm. On the other hand, the SSHAs along the coast of Japan calculated by the OGCM reach 50 mm at most, suggesting that the Rossby wave signal arriving at the coast is smoothed by CTWs and other effects. This is consistent with the fact that the regression of EOF1 to SSH in the open sea is much larger than that along the coast (Fig. 6).

4.2.2 CTW experiments

We will examine how the EOF1, which raises the SSHAs of the whole Japan coast, is created by CTWs. There are two leading candidates as excitation sources for the CTWs. One is the baroclinic Rossby wave reaching off Hokkaido in the northern latitudes of the Kuroshio Extension as seen in the 1.5-layer model experiment. The other is the large-scale SSHA pattern at the latitudes of the Kuroshio Extension, which leads to the north-south anomaly of the Kuroshio, and thus the SSHAs concentrated near the Kuroshio reaches the

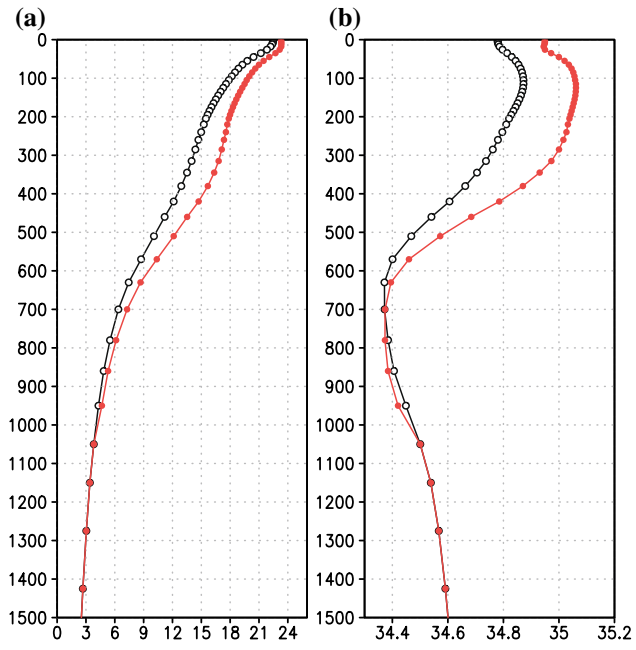

Fig. 11 Vertical profile of initial and reference state. **a** The black line shows the vertical profile of the initial temperature (θ_i) and the red line shows that of the reference temperature (θ_r). **b** Same as **a** but for salinity. Unit of (a) is °C, and that of **b** is psu

coast of Japan as in the previous studies (Sasaki et al. 2014, Usui et al. 2021). To determine which of these sources is more suitable as a CTWs excitation source for making the EOF1 pattern, we perform idealized experiments with these two excitation sources as forcing.

The model used in the idealized experiments is the same NP model, but with a smaller domain and no nesting procedure. The initial state is a uniformly stratified state (Fig. 11). We conducted two experiments: one with a positive SSHAs off the east coast of Hokkaido (exp Hokkaido) and the other with a positive SSHAs off the Boso Peninsula (exp Boso). We will examine which response to the external forcing is more appropriate as a signal for the EOF1. The local SSHAs are created by relaxing the local model temperature/salinity to the reference temperature/salinity through the experiments as follows,

$$F_\theta = -a(\theta - \theta_r), \tag{8}$$

$$F_s = -a(s - s_r), \tag{9}$$

where a is the restoring coefficient (Figs. 12c–d), θ, and s are the potential temperature and salinity in the model and subscript r means their referenced values (Fig. 12a–b). To allow a free response on the continental shelf (<200 m depth), body forcing is applied only in the open ocean (>200 m depth). This method of examining the sensitivity of uniform stratification to local body forcing has also been used by Tsujino et al. (2008). In addition, similar to Tsujino et al. (2008), the coefficient of the horizontal viscosity is increased in the Tsugaru Strait and the southern coast of Japan so that CTWs are partially blocked in these areas (Table 3). This roughly represents the horizontal viscosity created by the shear and strain of the background velocity field not expressed in the CTW experiments. The conclusion here does not depend much on the value of this viscosity coefficient.

Table 3 Coefficient of horizontal viscosity in experiment CTW. Unit is $m^2\ s^{-1}$

Tsushima	Tsugaru	Soya	South of Japan
7.0×10^3	3.0×10^3	3.0×10^3	5.0×10^3

Similar experiments to exp Hokkaido may correspond to the experiments in which anomalies are given off Sakhalin in Tsujino et al. (2008) and Kida et al. (2016). They targeted the seasonal variability of the Tsushima Current, and we examine the correspondence with the pattern of the EOF1 on the multidecadal scale. Similar experiments to exp Boso have been conducted in Sasaki et al. (2017) and Usui et al.

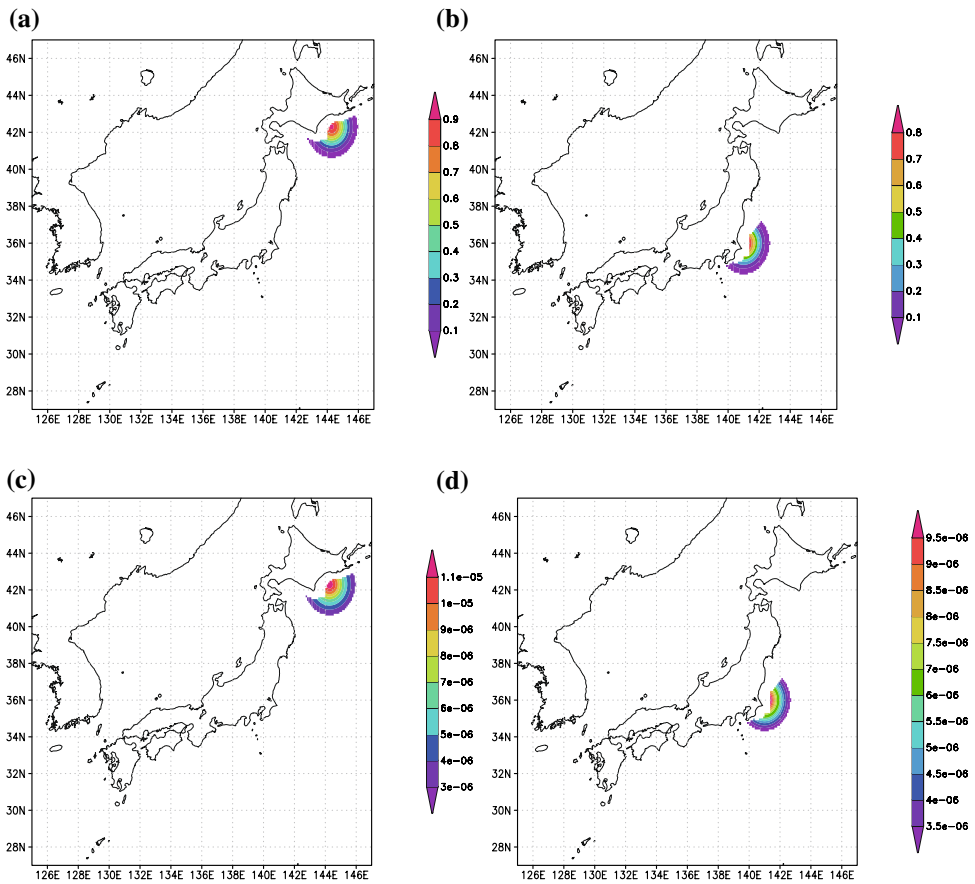

Fig. 12 **a** Horizontal map of the difference between the reference temperature (θ_r) and initial temperature (θ_i), $\theta_r - \theta_i$, at the surface for exp Hokkaido. Unit is °C. **b** Same as **a** but for exp Boso. **c** Horizontal map of restoring coefficient (a in Eq. (9)) for exp Hokkaido. Unit is s^{-1}. **d** Same as **c** but for exp Boso

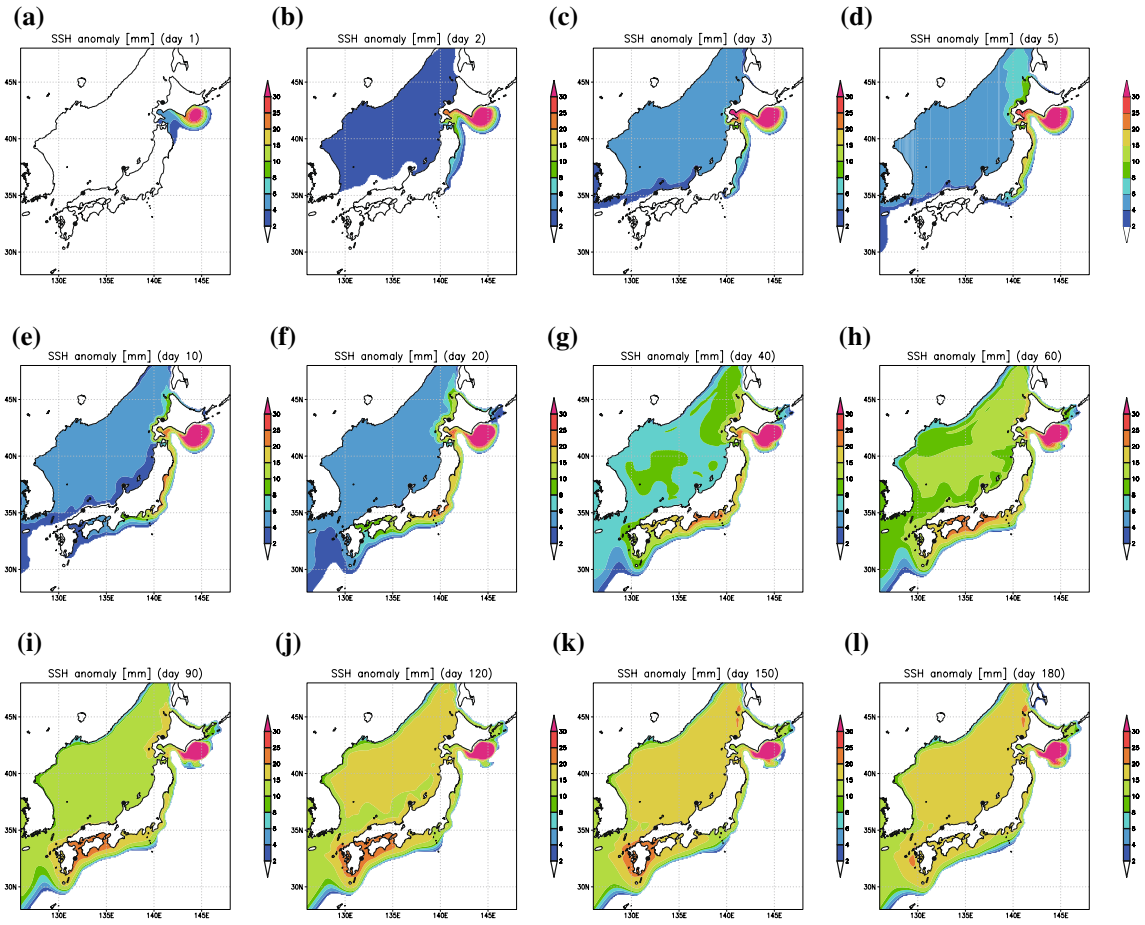

Fig. 13 SSHAs for exp Hokkaido. Unit is mm. **a** day 1, **b** day 2, **c** day 3, **d** day 5, **e** day 10, **f** day 20, **g** day 40, **h** day 60, **i** day 90, **j** day 120, **k** day 150, and **l** day 180

(2021) as anomalies created when the Kuroshio approaches Japan.

The time series of SSHA are presented for exp Hokkaido in Fig. 13, and for exp Boso in Fig. 14. In exp Hokkaido, after reaching the Tsugaru Strait (Fig. 13a, b), the signals are divided into two: one crossing the Tsugaru Strait to the west coast of Hokkaido, and the other moving southward along the east coast of Honshu. When the former signal, which crosses the Tsugaru Strait and is transmitted to the west coast of Hokkaido, reaches the Sea of Japan, a uniform SSHA rise is observed over the entire Sea of Japan in a single day (Fig. 13b). This suggests that the response is the adjustment due to barotropic Rossby waves, as shown by Kida et al. (2016) and others. It will be shown later that this uniform response in the Japan Sea is actually due to the barotropic component of SSHA by dividing the data into (local) steric and non-steric components (Eqs. 10 and 11). The southward signal along the Pacific Coast of Tohoku reaches the Boso Peninsula and thereafter moves along the southern coast of Honshu and Kyushu (Figs. 13c–e). From the southern tip of Kyushu, the signal passes along the northern coast of Kyushu and reaches the Sea of Japan (Fig. 13f). As it moves northward along the west coast of Kyushu, the East China Sea and the Sea of Japan show an immediate response due to the barotropic Rossby wave (Fig. 13f), just as when the CTWs that crossed the Tsugaru Strait ejected the forward Rossby wave into the Sea of Japan (Fig. 13c).

The fastest propagation of signal is about 3 m/s as CTWs, looking right at the shore. This speed is almost consistent with the CTWs of the first mode. There is also slow signal propagation that is consistent with the second and third modes. To elucidate the propagation of CTW, fast and slow arrival times of the CTW signal are estimated at the 77 tide gauge stations as time required for the SSHA value to reach 0.1 and 0.5 times its 180th day value (Fig. 15), respectively. In exp Hokkaido, the signal arrives fast at a large part of the Japan Sea coast through the Tsugaru Strait within 3 days due to the barotropic Rossby wave transmitted to the west coast of Hokkaido through the Tsugaru Strait as mentioned before (Figs. 13c and 15a). The signal propagates along the southern coast of Japan and reaches the northern coast of

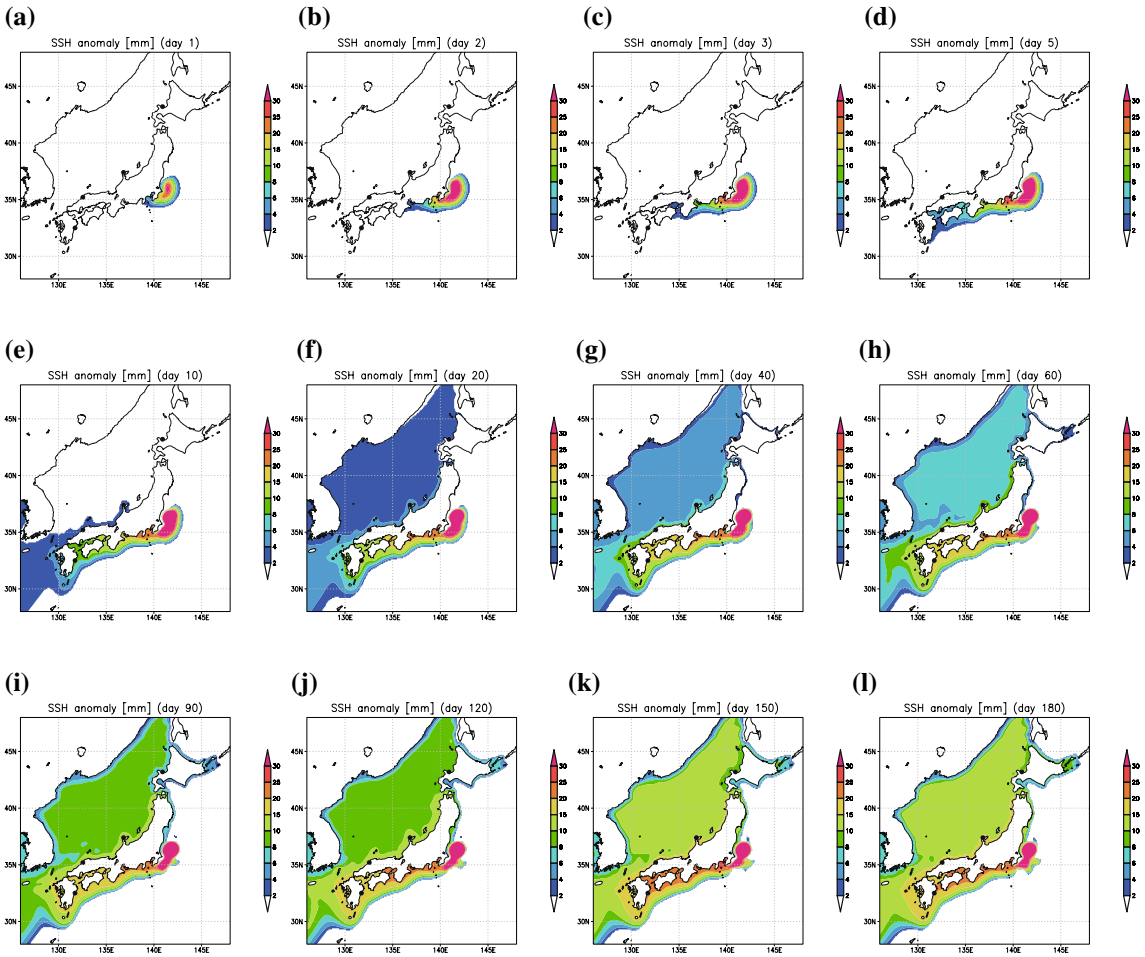

Fig. 14 Same as Fig. 13 but for exp Boso

Kyushu within the 13 days (Figs. 13e and 15a). The slow arrival time along the Japan Sea in exp Hokkaido is more than 40 days (Figs. 15c and d).

In exp Boso, the fast signal reaches the north coast of Kyushu on the 10th day (Figs. 14c and 15b). This is consistent with the time it takes for the Kuroshio origin signal off the Boso Peninsula to reach the Japan Sea by the CTW first mode in shown by Usui et al. (2021). The interior of the Japan Sea is then transmitted almost simultaneously (Figs. 14f and 15b). The fast arrival time of Pacific Coast of Tohoku and Hokkaido is more than 15 days (Figs. 15b), and the slow arrival time along the Tohoku and Hokkaido is more than 40 days (Figs. 15c and d).

After 150 or 180 days, the SSHA reaches an almost stationary state (Figs.13 k and l). In exp Hokkaido, the signal is almost uniform around the four main islands but it is weaker in the eastern part of Hokkaido (Fig. 16a), where the anomaly forcing is applied. The reason why the SSHA signal is relatively low along the eastern side of Hokkaido is as follows. The high SSHA signal just east of Hokkaido induce anticyclonic geostrophic flow there, requiring a northward compensation flow on the east coast of Hokkaido. The presence of the northward flow results in relatively low SSHAs just west of the high SSHAs due to geostrophic relation. The equation for this phenomena is derived by Minobe et al. (2017)(their Fig. 2) on a steep beach and by Wise et al. (2018) on the seafloor slope. In exp Boso, the positive anomalies are smaller at the Pacific side of Tohoku and Hokkaido. A comparison at the tide gauge between exp Hokkaido and exp Boso shows that exp Hokkaido is more similar to the EOF1 in terms of uniform positive anomalies around Japan with smaller anomalies at the eastern side of Hokkaido (Figs. 16a, b).

The next question is why CTWs can travel to the entire main Japan islands in the case of exp Hokkaido, whereas only part of CTWs arrives late to Hokkaido and Tohoku in the case of exp Boso. As an extreme example of this, we conduct supplementary experiments where there is no viscosity in the Tsugaru strait (exp no-visc Hokkaido and exp no-visc Boso). In exp no-visc Boso, the values are consistently high

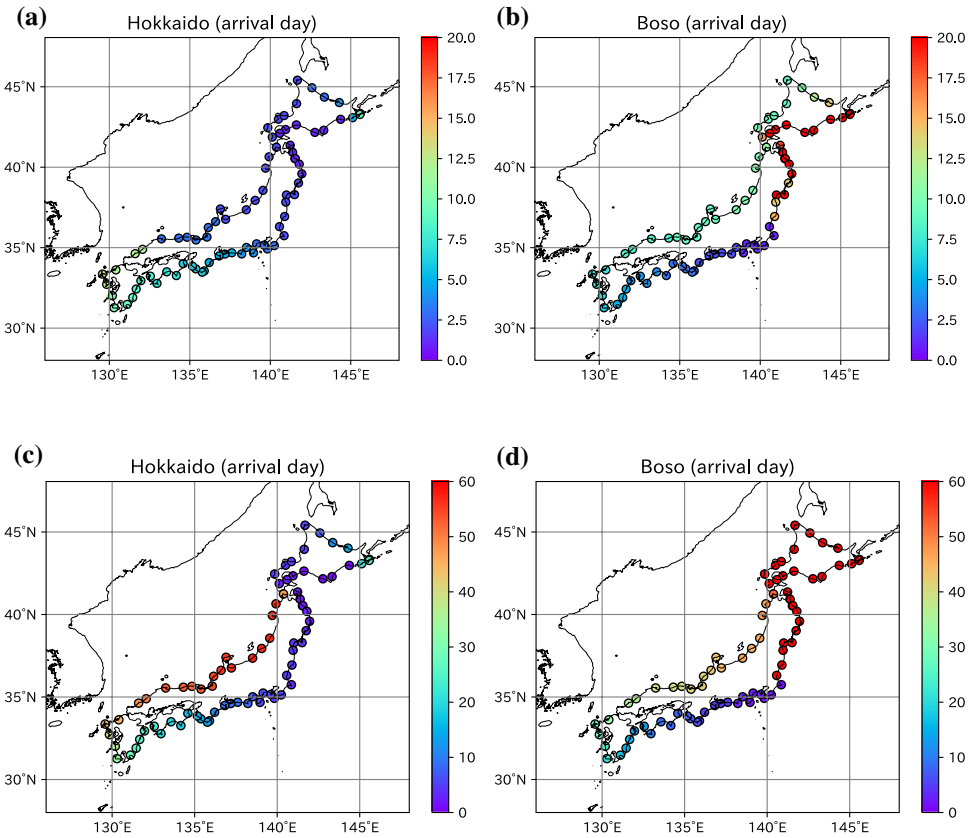

Fig. 15 Fast (**a**, **b**) and slow (**c**, **d**) arrival times for exp Hokkaido (**a**, **c**) and exp Boso (**b**, **d**). The fast and slow arrival times are estimated as the time it takes for SSHA values to reach 0.1 (fast) and 0.5 (slow) times the 180-day value at the 77 tide gauge station, respectively

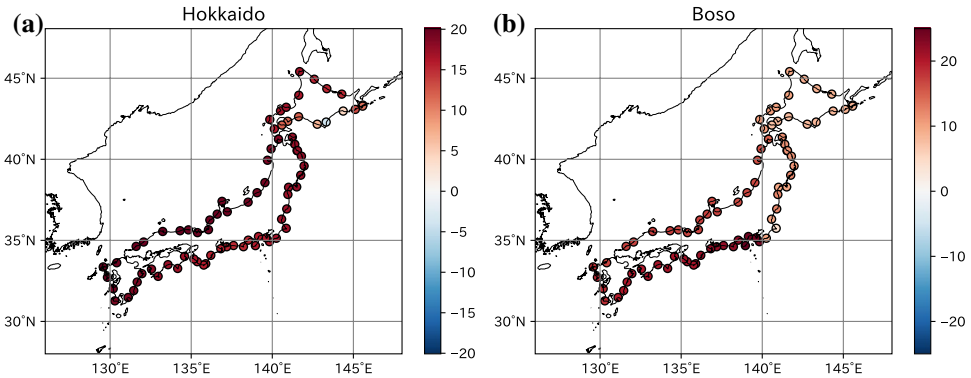

Fig. 16 SSHAs in day 180 at the 77 tide gauge stations (open circles) for (**a**) exp Hokkaido and (**b**) exp Boso. Unit is mm

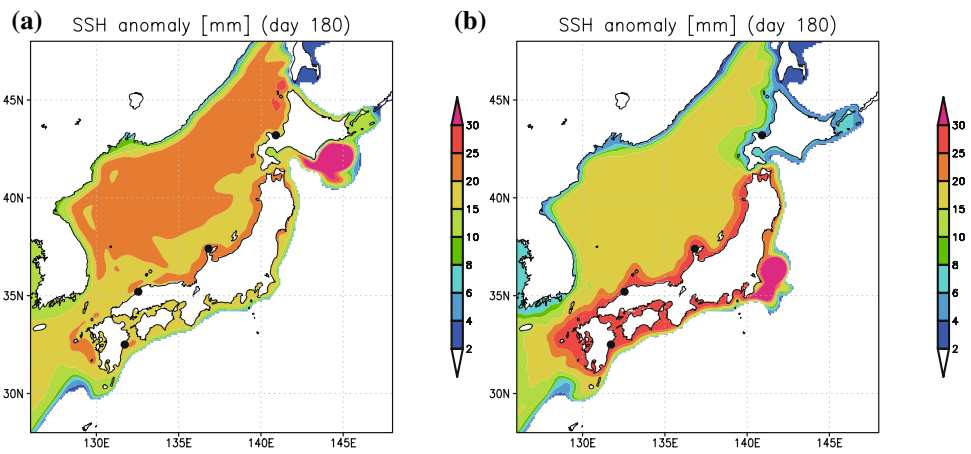

Fig. 17 Same as Figs. 13l and 14l but for (**a**) exp no-visc Hokkaido and (**b**) exp no-visc Boso

along Honshu, Shikoku, and Kyushu and in the East China Sea and the Japan Sea, but Hokkaido is excluded (Fig. 17). In the case of exp no-visc Hokkaido, there is not much of a difference between the no-visc and normal cases. This indicate that the Tsugaru Strait is a determinant factor and the viscosity acts as a supplement. Thus, in the absence of viscosity, high SSHAs east of Hokkaido travels to Honshu in exp Hokkaido, whereas high SSHAs east of Honshu do not travel to Hokkaido in exp Boso.

To consider the reasons for the difference between exp Hokkaido and exp Boso, we divide the SSHA into (local) steric and non-steric components, as Usui et al. (2021) did.

$$(\text{steric}) = -\frac{1}{\rho_0}\int_{-H}^{\eta}\Delta\rho(\theta,s,z)dz, \tag{10}$$

$$(\text{non-steric}) = \text{SSHA} - (\text{steric}), \tag{11}$$

where ρ_0 is the reference density, H is the ocean depth, and η is the surface height. The steric and non-steric components are associated with baroclinic and barotropic components.

In exp Hokkaido, the forcing signal east of Hokkaido is directly connected with the strong steric component that appears deeper than 200 m along the continental shelf from southeastern Hokkaido to southern Kyushu (Fig. 18a). Therefore, the forcing signal directly propagates from Hokkaido to Honshu over the Tsugaru strait (Fig. 19a). On the other hand, in exp Boso case, the large steric component that is directly connected with the forcing is present only from the Boso Peninsula to the west, resulting in weak signal in Hokkaido and Honshu north of the Boso Peninsula (Figs. 18b and 19b).

In places where the steric component cannot directly reach, such as the region north of the Boso Peninsula in exp Boso and the Japan Sea in both experiments, weak steric component is only seen on the continental shelf. This steric component on the continental shelf is considered to be the propagation of the second or third modes of CTW, which has a larger steric signal on the continental shelf than the first mode (Fig. 12 of Usui et al. (2021) and others). The slow arrival is considered to be due to these modes.

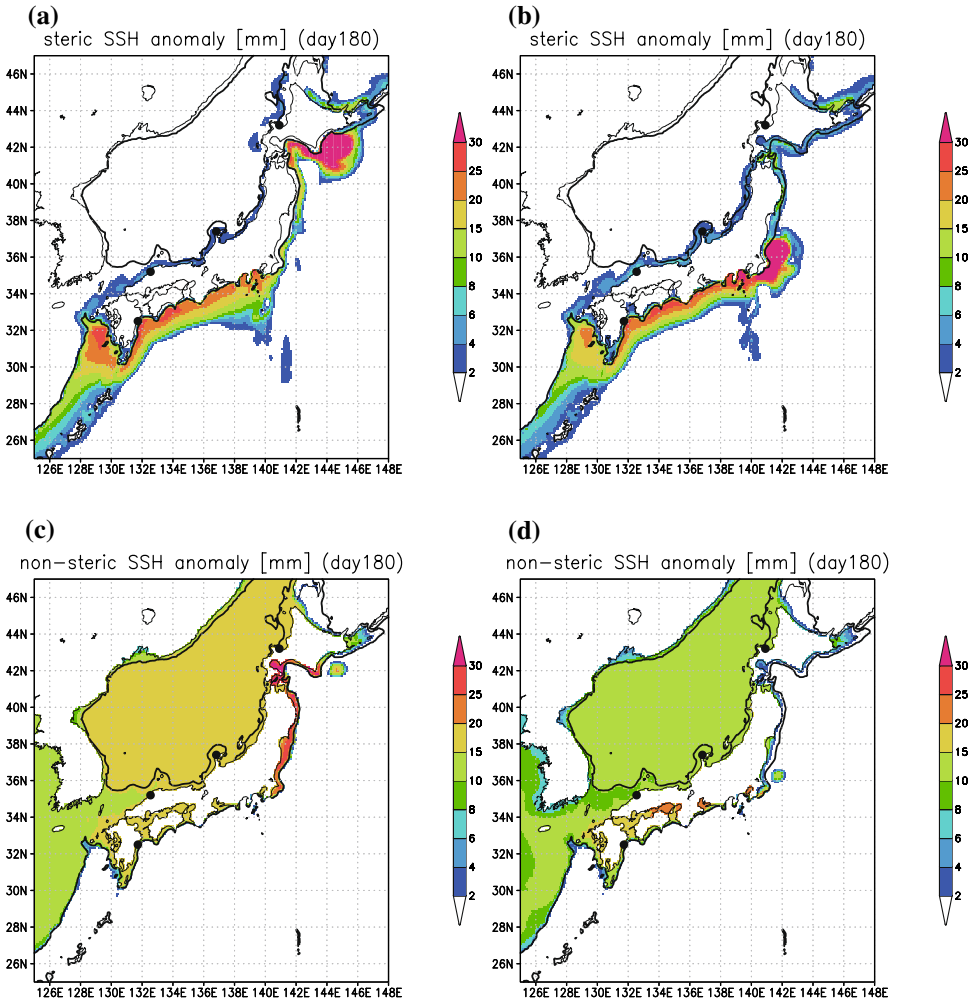

Fig. 18 Steric (**a**, **b**) and non-steric (**c**, **d**) components of SSHAs at day 180 for (**a**, **b**) exp Hokkaido and (**b**, **d**) exp Boso. Black lines indicate the 200 m isobath. Unit is mm

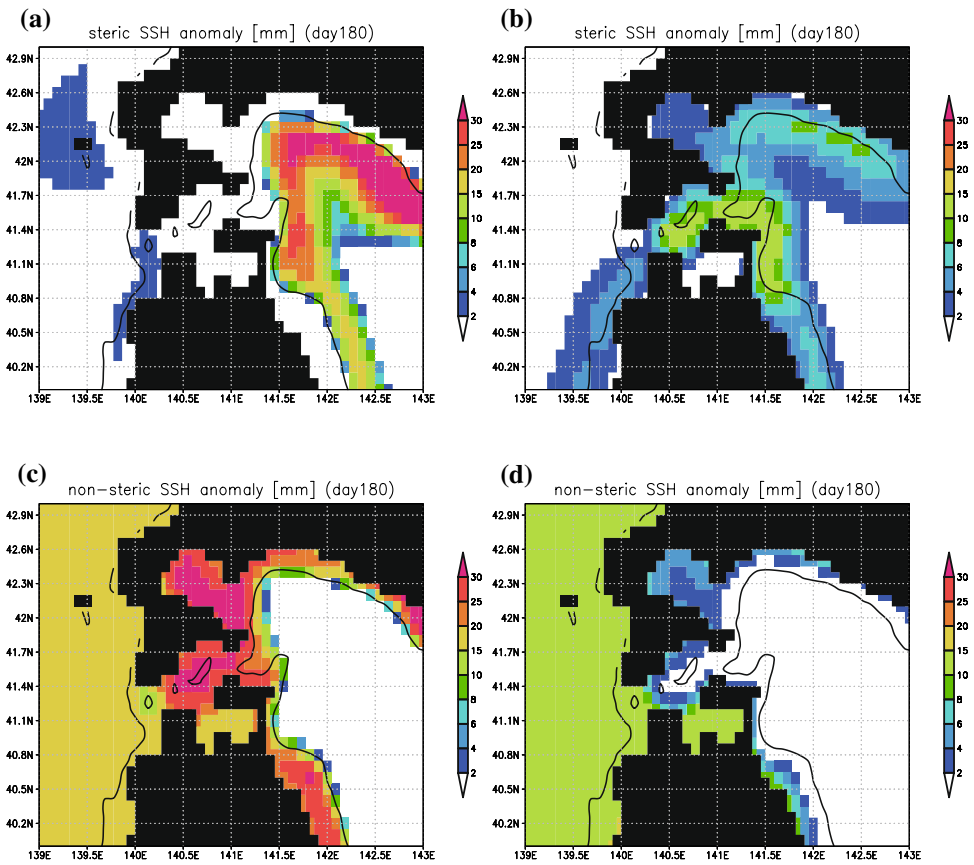

Fig. 19 Same as Fig. 18 but shown on an enlarged map around the Tsugaru Strait

Figure. 18c, d show the non-steric component of exp Hokkaido and exp Boso. The non-steric component of the same strength as the adjacent steric component appears shallower than 200 m along the steric component on the continental shelf of the Pacific. Since the tide gauge station is located on the coast, the SSHA values correspond to this non-steric component on the Pacific coast. In the Japan Sea and the East China Sea, the non-steric component dominates both in the open ocean and on the continental shelf. This is consistent with the barotropic response of CTW in the Japan Sea as mentioned before. The fast arrival time in the Japan Sea is due to this barotropic CTW.

In conclusion for the CTW experiments, it is not possible to produce a distribution of positive anomaly including Hokkaido unless SSHAs due to steric component are applied along Hokkaido. In addition, as the EOF1 of the hindcast experiments, SSHAs in exp Hokkaido are relatively low along the southeastern part of the Hokkaido. These similarities suggest that exp Hokkaido is more appropriate to explain the SSHAs in the 1950s than exp Boso. However, a closer look at EOF1 shows that the signal south of Honshu is slightly stronger, suggesting that the exp Boso signal also contributes to some extent.

5 Summary and discussions

To investigate the long-term variability of sea level anomalies along Japan (JPN-SLAs) during the 20th century, we conducted two hindcast experiments using a model capable of representing realistic Kuroshio Extension and coastal trapping waves (CTWs) with two sets of reanalysis data through the 20th century, and compared them with the tide gauge estimate. Note that the estimate by tide gauge station corresponds to the relative JPN-SLAs, that is, the anomalies in local mean sea level relative to the vertical land movements (VLMs) at the tide gauge station.

The relative JPN-SLAs did not show long-term trend throughout the 20th century (Table 2), accompanying a predominant 50-year cycle with a distinct peak in the 1950s, whereas the modeled JPN-SLAs and global averaged SLAs show a consistent upward trend with a multidecadal variation. To investigate this difference, we calculate time series of the standard deviation at each tide gauge from their mean. Standard deviations from the model range from 5 to 20 mm throughout the period, while those from tide gauge show larger temporal variability. The latter is comparable to the former

around 1995, but increases away from the period. The effect of VLMs is thought to be a major factor for this. If this conclusion is correct, combined with the barystatic estimated of Frederikse et al. (2020), then this model estimate (1.79 [0.89~2.28] for 1900–2100, Table 2) corresponds to the JPN-SLAs without VLMs, which are close to the global averaged SLAs estimated in recent studies (IPCC 2021).

Next, we examined the mechanism of the relatively high JPN-SLAs in the 1950s, which are the most prominent multidecadal signal in both tide gauge estimate and model by examining sea surface height anomalies (SSHAs) to focus on dynamic variability. The empirical orthogonal function (EOF) analysis for the 5-year running-mean SSHAs for 1920–1970 shows that the first EOF (EOF1) is dominant with the peak in the 1950s. It is confirmed that high SSHAs signal comes from the central Pacific as baroclinic Rossby waves created by the wind stress, which is consistent with the finding of Sasaki et al. (2017). To elucidate how the SSHAs in the open ocean create the SSHAs along Japan through the adjustment of CTWs, we conducted two idealized experiments that are forced by the anomalies in two locations: one is east of Hokkaido, as suggested by the shallow water model, and the other is off the Boso Peninsula, as suggested by the EOF1 regression. From the idealized experiments, the former experiment explained the pattern of EOF1 better than the latter one in terms of uniform positive anomalies around Japan with smaller anomalies at the eastern side of Hokkaido. The reason for this is that the external forcing signal has a large steric component and propagates along the continental shelf deeper than 200 m to the right of land. When the signal is applied east of Hokkaido, this steric component can propagate directly across the Tsugaru Strait to the entire south coast of Japan, but when the signal is applied off the Boso Peninsula, this steric component propagates only to the west of Boso and not directly to the Pacific coast of Hokkaido and Tohoku.

Lastly, we make a remark on representative errors of the model. Because this model only marginally represents the continental shelves, it may underestimate SLAs associated with small spatio-temporal scale phenomenon along the coast. However, the standard deviation in the model is comparable to that in the tide gauge observation in the 1990s (Fig. 4), which is the middle period of the reference period 1980–2010, where the effect of VLMs is considered to be small and oceanographic phenomenon is expected to be dominant (Eq. 7). This similarity at this period indicates that the modeled σ_0 is comparable to that of the observation. Accordingly the problem of the representative errors in the hindcast experiments seems not a serious problem in estimating JPN-SLAs.

Appendix: Trend estimation

We compute noise parameters and the resulting trend and standard deviation (σ) using the Hector software (Bos et al. 2013) for each annual-mean time series of the SLAs components in exps 20CRv3 and ERA20C. The uncertainty of the trend is then defined as 1.64 times the standard deviation (corresponding to the 90% confidence interval). We assume that the spectrum of all time series can be approximated by a generalized Gauss Markov spectrum following Frederikse et al. (2020). Trend is estimated as the mean of these two experiments. We count for their trend errors by adding the half of difference in trends and uncertainties calculated in the Hector software in quadrature. The trend of the barystatic component estimated by Frederikse et al. (2020) and its uncertainty is calculated using their python scripts. Total trend is the sum of the steric, dynamic, and barystatic trends. The uncertainties are added in quadrature.

We also estimate the linear trend of the tide gauge observation using the Hector software for the four tide gauges stations assuming the AR(1) (first-order autoregressive) noise model. We count for their trend errors by adding the standard deviation of the estimated trends for the four stations and their uncertainties calculated in Hector software in quadrature.

Acknowledgements 20th Century Reanalysis V3 data provided by the NOAA/OAR/ESRL PSL, Boulder, Colorado, USA, from their Web site at https://psl.noaa.gov/data/gridded/data.20thC_ReanV3.html. ERA20C data is provided by ECMWF form their bweb site at https://www.ecmwf.int/en/forecasts/datasets/reanalysis-datasets/era-20c. Dr. Usui gave us useful advice on CTW analysis. The EOF analysis was performed using a python library developed by Dawson (2016). Linear trends are calculated by the Hector software (Bos et al. 2013). This work is funded by MRI and is partly supported by JSPS KAKENHI Grant Number JP19H05701. Part of graphics was produced with the Grid Analysis and Display System (GrADS).

References

Bos MS, Fernandes R, Wiliams SDP, Bastos ML (2013) Fast error analysis of continuous GNSS observations with missing data. J Geod 87:351–0360. https://doi.org/10.1007/s00190-0121-0605-0

Boyer TP, Antonov JI, Baranova OK, Coleman C, Garcia HE, Grodsky A, Johnson DR, Locarnini RA, Mishonov AV, O'Brien TD, Paver CR, Seidov D, Smolyar IV, Zweng MM (2013) World Ocean Database 2013, NOAA Atlas NESDIS 72, S. Levitus, Ed., A. Mishonov, Technical Ed.; Silver Spring, MD, 209 pp., https://doi.org/10.7289/V5NZ85MT

Dawson A (2016) A library for EOF analysis of meteorological, oceanographic, and climate data. J Open Res Softw 4:e14. https://doi.org/10.5334/jors.122

Frederikse T, Landerer F, Caron L, Adhikari S, Parkes D, Humphrey VW, Dangendorf S, Hogarth P, Zanna L, Cheng L, Wu YH (2020) The causes of sea-level rise since 1900. Nature 584:393–397. https://doi.org/10.1038/s41586-020-2591-3

Greatbatch RJ (1994) A note on the representation of steric sea level in models that conserve volume rather than mass. J Geophys Res 99:12767–12771

Gregory JM, Griffies SM, Lowe Hughes CW, JA, Church JA, Fukimori I, Gomez N, Kopp RE, Landerer F Le Cozannet G, Ponte RM, Stammer D, Tamisiea ME, van de Wal, RSW (2019) Concepts and terminology for sea level: mean, variability and change, both local and global. Surv Geophys 40:1251–1289. https://doi.org/10.1007/s10712-019-09525-z

Griffies SM, Greatbatch RJ (2012) Physical processes that impact the evolution of global mean sea level in ocean climate models. Ocean Model 51:37–72. https://doi.org/10.1016/j.ocemod.2012.04.003

Griffies SM, Hallberg RW (2000) Biharmonic friction with a Smagorinsky-like viscosity for use in large-scale eddy-permitting ocean models. Mon Wea Rev 128:2935–2946. https://doi.org/10.1175/1520-0493(2000)128<2935:BFWASL>2.0.CO;2

Hammond WC, Blewitt G, Kreemer C, Nerem RS (2021) GPS Imaging of global vertical land motion for studies of sea level rise. J Geophys Res Solid Earth, 126:e2021JB022355. https://doi.org/10.1029/2021JB022355

Hughes CW, Fukumori I, Griffies SM, Huthnance JM, Minobe S, Spence P, Thompson KR, Wise A (2019) Sea level and the role of coastal trapped waves in mediating the influence of the open ocean on the coast. Surveys Geophys 40:1467–1492. https://doi.org/10.1007/s10712-019-09535-x

Hunke EC, Dukowicz JK (1997) An elastic-viscous-plastic model for sea ice dynamics. J Phys Oceanogr 27:1849–1867. https://doi.org/10.1175/1520-0485(1997)027<1849:AEVPMF>2.0.CO;2

Hunke EC, Dukowicz JK (2002) The elastic-viscous-plastic sea ice dynamics model in general orthogonal curvilinear coordinates on a sphere: Incorporation of metric terms. Mon Wea Rev 130:1848–1865. https://doi.org/10.1175/1520-0493(2002)130<1848:TEVPSI>2.0.CO;2

IPCC 2019: IPCC Special Report on the Ocean and Cryosphere in a Changing Climate. Cambridge University Press. *in press*

IPCC (2021) Climate Change 2021: The Physical Science Basis. Contribution of Working Group I to the Sixth Assessment Report of the Intergovernmental Panel on Climate Change. Cambridge University Press. *in press*

Ishizaki H, Yamanaka G (2010) Impact of explicit sun altitude in solar radiation on an ocean model simulation. Ocean Modell 33:52–69. https://doi.org/10.1016/j.ocemod.2009.12.002

Jevrejeva S, Palanisamy H, Jackson LP (2021) Global mean thermosteric sea level projections by 2100 in CMIP6 climate models. Environ Res Lett 16:014028. https://doi.org/10.1088/1748-9326/abceea

JMA (2004) Ocean health assessment chart (2004), 35–43.(in Japanese)

JMA (2013) Ocean health assessment chart (2013), 59–68.(in Japanese)

JMA (2020) Climate Change in Japanese (2020) (in Japanese) https://www.data.jma.go.jp/cpdinfo/ccj/index.html

Kato T, Tsumura K (1979) Vertical land movement in Japan as deduced from tidal record (1951–1978). Bull Earthquake Res Inst 54:559–628 (**(in Japanese)**)

Kato T (1983) Secular and earthquake-related vertical crustal movements in Japan as deduced from tidal records (1951–1981). Tectonophysics 97(1983):183–200

Kida S, Qiu B, Yang J, Lin X (2016) The annual cycle of the japan sea throughflow. J Phys Oceanogr 46:23–39

Kiss amnd coauthors (2020) ACCESS-OM2 v1.0: a global ocean-sea ice model at three resolution. Geosci Model Dev 13:401–442 https://doi.org/10.5194/gmd-13-401-2020

Kusahara K (2020) Interannual-to-multidecadal responses of Antarctic ice shelf-ocean interaction and coastal water masses during the twentieth century and the early twenty-first century to dynamic and thermodynamic Forcing. J Clim 33:4941–4973

Large WG, Yeager SG (2004) Diurnal to decadal global forcing for ocean and sea-ice models: The data sets and flux climatologies. NCAR Tech. Note: TN-460+STR, CGD Division of the National Center for Atmospheric Research

Mellor GL, Ezer T (1995) Sea level variations induced by heating and cooling: an evaluation of the Boussinesq approximation in ocean models. J Geophys Res 100:20565–20577

Mellor GL, Kantha L (1989) An ice-ocean coupled model. J Geophys Res 94:10937–10954. https://doi.org/10.1029/JC094iC08p10937

Merryfield WJ, Holloway G (2003) Application of an accurate advection algorithm to sea-ice modelling. Ocean Modell 5:1–15. https://doi.org/10.1016/S1463-5003(02)00011-2

Minobe S, Terada M, Qiu B, Schneider N (2017) Western boundary sea level: A theory, rule of thumb, and application to climate models. J Phys Oceanogr 47:957–977. https://doi.org/10.1175/JPO-D-16-0144.1

Okumura Y, Hirahara T (2016) Long-term trends in sea level change along the coast of Japan -A review of recent studies and Corrections Using Ground Motions from GPS Observations (in Japanese). Sokko-Jiho 83:S21–S31

Naito R, Asai T, Kawaguchi K, Inomata T, Tsutumi D, Narita K (2015) Estimation of Sea level rise using the tide gauge records in the port areas and their characteristics (in Japanese), Technical Note of NILIM 855 June 2015 (YSK-N-316)

Nakano H, Matsumura Y, Tsujino H, Urakawa S, Sakamoto K, Toyoda T, Yamanaka G (2021) Effects of eddies on the subduction and movement of water masses reaching the 137°E section using Lagrangian particles in an eddy-resolving OGCM. J Oceanogr 77:283–305. https://doi.org/10.1007/s10872-020-00573-3

Nyomura, Marine Meteorological Observatories and Kobe Collection (in Japanese), Seibundo Shoten

Poli P (2016) ERA-20C: An atmospheric reanalysis of the twentieth century. J Clim 29:4083–4097. https://doi.org/10.1175/JCLI-D-15-0556.1

Prather MJ (1986) Numerical advection by conservation of second-order moments. J Geophys Res 91:6671–6681. https://doi.org/10.1029/JD091iD06p06671

Sakamoto K, Tsujino H, Nakano H, Urakawa S, Toyoda T, Hirose N, Usui N, Yamanaka G (2019) Development of a 2km-resolution ocean model covering the coastal seas around Japan for operational application. Ocean Dyn 69:1181–1202

Sasaki YN, Minobe S, Miura Y (2014) Decadal sea-level variability along the coast of Japan in response to ocean circulation changes. J Geopys Res 119:265–275. https://doi.org/10.1002/2013JC009327

Sasaki YN, Washizu R, Yasuda T, Minobe S (2017) Sea level variability around Japan during the twentieth century simulated by a Regional Ocean Model. J Phys Oceanogr 30:5585–5595. https://doi.org/10.1175/JCLI-D-16-0497.1

Senjyu T, Matsuyama M, Matsubara N (1999) Interannual and decadal sea-level variations along the Japanee coast. J Oceanogr 55:619–633

Slivinski LC, coauthors, (2019) Towards a more reliable historical reanalysis: Improvements for version 3 of the Twentieth Century Reanalysis system. Q J R Meteorol Soc 145:2876–2908. https://doi.org/10.1002/qj.3598

Suzuki T, Yamazaki D, Tsujino H, Komuro Y, Nakano H, Urakawa S (2018) A dataset of continental river discharge based on JRA-55 for use in a global ocean circulation model. J Oceanogr 74:421–429. https://doi.org/10.1007/s10872-017-0458-5

Tamisiea ME, Mitrovica JX (2011) The moving boundaries of sea level change: Understanding the origins of geographic variability. Oceanography 24(2):24–39. https://doi.org/10.5670/oceanog.2011.25

Tsujino H, Nakano H, Motoi T (2008) Mechanism of currents through the straits of the japan sea: mean state and seasonal variation. J Oceanogr 64:141–161

Tsujino H, Nakano H, Sakamoto K, Urakawa S, Hirabara M, Ishizaki H, Yamanaka G (2017) Reference manual for the Meteorological Research Institute Community Ocean Model version 4 (MRI. COMv4). Tech Rep. 80, Meteorological Research Institute, Japan, https://doi.org/10.11483/mritechrepo./80

Tsujino H, Urakawa S, Nakano H, Small RJ, Kim WM, Yeager SG, Danabasoglu G, Suzuki T, Bamber JL, Bentsen M, Böning C, Bozec A, Chassignet EP, Curchitser E, Dias FB, Durack PJ, Griffiesn SM, Harada Y, Ilicak M, Josey SA, Kobayashi C, Kobayashi S, Komuro Y, Large WG, Le Sommer J, Marsland SJ, Masinas S, Scheinert M, Tomita H, Valdivieso M, Yamazaki D (2018) JRA-55 based surface dataset for driving ocean-sea-ice models (JRA55-do) Ocean Modelling 130:79–139 https://doi.org/10.1016/j.ocemod.2018.07.002

Umlauf L, Burchard H (2003) A generic length-scale equation for geophysical turbulence models. J Marine Res 61:235–265. https://doi.org/10.1357/002224003322005087

Usui N, Ogawa K, Sakamot K, Tsujino H, Yamanaka G, Kuragano T, Kamachi M (2021) Unusually high sea level at the south coast of Japan in September 2011 induced by the Kuroshio. J Oceanogr 77:447–461. https://doi.org/10.1007/s10872-020-00575-1

Yamanaka G, Nakano H, Sakamoto K, Toyoda T, Urakawa S, Nishikawa S, Wakamatsu T, Tsujino H, Ishikawa Y (2021) Projected climate change in the western North Pacific at the end of the 21st century from ensemble simulations with a high-resolution regional ocean model. J Oceanogr 77:539–560. https://doi.org/10.1007/s10872-021-00593-7

Wise A, Hughes CW, Polton JA (2018) Bathymetric Influence on the Coastal Sea Level Response to Ocean Gyres at Western Boundaries. J Phys Oceanogr 48:2949–2964. https://doi.org/10.1175/JPO-D-18-0007.1